



Review

Modelling optical properties of atmospheric black carbon aerosols

Michael Kahnert^{a,b,*}, Franz Kanngießer^b^a Research Department, Swedish Meteorological and Hydrological Institute, Folkborgsvägen 17, Norrköping SE-601 76, Sweden^b Department of Space, Earth and Environment, Chalmers University of Technology, Gothenburg SE-412 96, Sweden

ARTICLE INFO

Article history:

Received 2 December 2019

Revised 21 January 2020

Accepted 21 January 2020

Available online 22 January 2020

Keywords:

Atmospheric optics

Aerosol

Black carbon

Brown carbon

ABSTRACT

The optical properties of atmospheric black carbon (BC) aerosols are needed to model the direct radiative forcing of the climate system, as well as for interpreting and assimilating remote sensing observations from satellites. Modelling efforts during the past decade have predominantly been based on using morphologically highly realistic representations of the particle geometry in conjunction with numerically exact methods for solving the light-scattering problem. We review (i) the present state of knowledge about the morphological, dielectric, and compositional properties of BC aerosols, (ii) the state-of-the-art in numerical light-scattering methods frequently applied to black carbon, and (iii) the recent literature on modelling optical properties of BC aggregates, both bare and internally mixed with liquid-phase material. From this review we formulate some key lessons learned regarding those morphological properties that have a dominant impact on the optical properties. These morphological key features can form the basis for devising simplified model particles that can be used in large-scale applications. We illustrate this approach with one example appropriate for climate modelling, and one example relevant to the interpretation of lidar remote sensing data.

© 2020 The Authors. Published by Elsevier Ltd.

This is an open access article under the CC BY license. (<http://creativecommons.org/licenses/by/4.0/>)

Contents

1. Introduction	2
2. Physical properties of black carbon	2
2.1. Morphology of bare black carbon particles	2
2.2. Morphology of coated black carbon particles	3
2.3. Size distribution	4
2.4. Dielectric properties	4
3. Computational methods	5
4. Optical properties of pure black carbon aggregates	6
5. Optical properties of black carbon aggregates mixed with liquid material	8
6. Toward a physical understanding of the relation between aerosol morphology and aerosol optics	11
7. Core grey shell (CGS) model for simulating optical cross sections of coated BC aggregates	11
8. Tunable model for simulating depolarisation by coated BC aggregates	12
9. Summary and recommendations	13
Declaration of Competing Interest	13
Acknowledgements	13
References	13

* Corresponding author.

E-mail addresses: michael.kahnert@smhi.se (M. Kahnert), franz.kanngieser@chalmers.se (F. Kanngießer).

1. Introduction

Black carbon (BC) aerosols are among the strongest radiative forcing agents in the atmosphere that can contribute to anthropogenic warming of the climate system [1–3]. Also, elevated concentrations of black carbon aerosols in ambient air are a public health concern [4], as they can cause allergies, pulmonary and cardiovascular diseases, and premature deaths (e.g. [5]). Thus, BC emission abatement measures have significant co-benefits for improving air quality and for counteracting climate warming on a short time scale [6].

A thorough understanding of the optical properties of BC particles is required for quantifying the radiative forcing effect of this type of aerosol (e.g. [7–9]). Incorrect or oversimplified assumptions about the particles' morphological properties can have a significant impact on the simulation of broadband radiative forcing rates in global models [10–12]. One important question is how to accurately represent the absorption enhancement caused by internal mixing with liquid-phase material (e.g. [13–16]).

Air quality models are frequently being constrained by assimilation of remote sensing observations (e.g. [17]). In chemical data assimilation an accurate description of aerosol optical properties is critical for making correct use of the information provided by the observations (e.g. [18,19]). A closely related problem is the inversion of ground based and satellite based remote sensing observations (e.g. [20]). One example are lidar profiles of the aerosol backscattering coefficient and depolarisation ratio (e.g. [21–24]). Differential scattering optical properties, such as those observed by lidar instruments, are significantly more sensitive to aerosol morphological properties than broadband radiative forcing rates. Thus, a comprehensive understanding of the optical properties of morphologically complex BC aerosols is even more essential in chemical data assimilation and remote sensing than in climate modelling.

A review of earlier work on light scattering by fractal aggregates can be found in [25]. Highly insightful overviews over current work on black carbon and its optical properties are found in two recent book chapters [26,27]. One goal of the present review is to distill from the present state of knowledge a microphysical understanding of the relation between morphological and optical properties. By identifying those microphysical features that have a dominant impact on the optical properties we can construct simplified model particles with a reasonable prospect of being utilised in large-scale applications, such as remote sensing retrievals, chemical data assimilation systems, and climate models.

The main focus in our review is on work done during the past decade on both bare and coated BC aerosols. The common theme in much of this work is an endeavour to understand the significance of various morphological features on the optical properties of BC aerosols. For this reason, we will start in Section 2 by reviewing our current state of knowledge of morphological properties of bare and coated black carbon particles, as well as their size distribution and dielectric properties. Accounting for morphological details in a model requires state-of-the-art methods for solving the light-scattering problem (e.g. [28,29]). Thus, we proceed in Section 3 with discussing numerical light-scattering methods suitable for application to BC aerosols. Optical properties of pure and coated BC particles are discussed in Sections 4 and 5, respectively. From this review, we make an attempt in Section 6 to draft a summary of our present physical understanding of the relation between BC morphology and optical properties. Based on this interpretation, we discuss two models that focus on what we presently regard to be the essential morphological features of BC; one model tailored to the needs of climate forcing computations (Section 7), and another for modelling depolarisation by coated aggregates (Section 8). In Section 9 we provide a brief

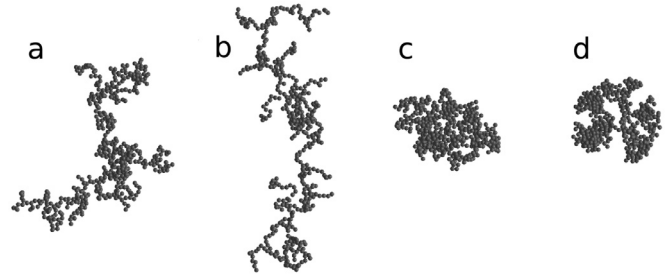


Fig. 1. Black carbon aggregates with varying fractal parameters; a: $D_f=1.8$, $k_0=1.3$; b: $D_f=1.8$, $k_0=0.7$; c and d: $D_f=2.4$, $k_0=0.7$. Geometries a–c were generated with the cluster-cluster aggregation algorithm, geometry d was produced with the diffusion-limited cluster aggregation algorithm.

summary and specific recommendations as a baseline for future work.

2. Physical properties of black carbon

2.1. Morphology of bare black carbon particles

Black carbon (BC) can be described as a fractal-like aggregate in which the aggregate size R and the number of primary particles (monomers) N_s are related by a power law $N_s \propto R^{D_f}$, where D_f denotes the Hausdorff dimension (or fractal dimension) [30]. More specifically, the canonical description of the fractal geometry of BC aggregates is given by the statistical scaling relation [31]

$$N_s = k_0 \left(\frac{R_g}{a} \right)^{D_f}, \quad (1)$$

where a is the monomer radius, k_0 is known as the fractal prefactor, and the radius of gyration is given by

$$R_g = \sqrt{\frac{1}{N_s} \sum_{i=1}^{N_s} (\mathbf{r}_i - \mathbf{r}_0)^2} \quad (2)$$

(see also the review in [32]). Here, \mathbf{r}_i denotes the position vector of the i th monomer, and \mathbf{r}_0 is the position of the aggregate's centre of mass. In this idealised description all monomers are homogeneous spheres with the same radius a , and neighbouring monomers are in point-contact with each other. The important point in this model is that the aggregates are assumed to be self-similar on different length scales. Thus, the scaling relation given in Eq. (1) applies not only to the aggregate as a whole, but also to any (sufficiently large) parts of the aggregate.

If the monomers can have different masses m_i , the radius of gyration is given by [33]

$$R_g = \sqrt{\frac{\sum_{i=1}^{N_s} (\mathbf{r}_i - \mathbf{r}_0)^2 m_i}{\sum_{i=1}^{N_s} m_i}}. \quad (3)$$

For polydisperse monomers the radius a in Eq. (1) needs to be replaced by the geometric mean of the monomers' radii.

As an illustration of the scaling law, Fig. 1 shows aggregates with different fractal properties (as indicated in the caption). All four aggregates consist of $N_s = 500$ monomers. Aggregates a and b both have fractal dimension $D_f = 1.8$, while c and d have $D_f = 2.4$. The aggregates with the lower fractal dimension are significantly more lacy than those with the higher fractal dimension. Aggregates a and b only differ in the fractal prefactor. The prefactor can be interpreted as a measure for the compactness of the aggregate branches. In the branches of aggregate b with a low prefactor ($k_0 = 0.7$) the branches form more linear chains as compared to those of aggregate a ($k_0 = 1.3$). Finally, aggregates c and

d have exactly the same fractal parameters. However, c has been constructed with the diffusion-limited cluster aggregation (DLCA) algorithm, while d has been formed with the diffusion-limited aggregation (DLA) algorithm (e.g. [31]). Both look rather similar, although c seems to have a more homogeneous distribution of the monomers throughout the aggregate. This illustrates that the geometry of the particles is not only defined by the set of parameters (N_s , a , D_f , k_0), but also by the algorithm used for constructing the model particles.

Aging [34,35] and embedding of BC in liquid-phase material [36–39] results in a compaction of the particles, i.e., an increase of the fractal dimension. Laboratory measurements indicate that this process can proceed on different time scales, depending on the coating material. But often the compaction process is largely completed when only very small amounts of coating material have been added onto the BC particle (see Fig. 4d in [40]). Further addition of coating material leads to a radial growth of the particles. The speed of restructuring process depends on the coating material [41–44]: rapid collapse [41,42], rapid collapse after reaching a threshold of coating volume [43], or slow collapse [44]. The compaction does not only depend on the volume of coating material, but in addition on the material's surface tension [45].

The fractal dimension of newly produced BC particles depends on the type of BC and the combustion conditions, but also on the method that is being employed for determining the fractal dimension from observations. For instance, for diesel soot values of D_f in the range 1.57–2.1 [46] and 2.1–2.9 [47] have been determined; the frequency distribution of fractal dimensions peaks around $D_f = 1.8$ –1.85 [48]. For Palas soot D_f lies in the range of 1.9–2.1 ([46]). In [39] values in the range of $D_f = 1.82$ –2.08 were observed. Soot aggregates formed in a spark-ignition engine showed fractal dimensions of $D_f = 2.2$ –3.0. More recent measurements based on 3D electron tomography with a transmission electron microscope [49] suggest that the fractal dimension is systematically underestimated by those techniques that are based on analysis of 2D images [50]. The 3D analysis yields D_f values for atmospheric BC particles near traffic emission sources in the range 2.1–2.3 with a median value of 2.2. The corresponding fractal prefactor k_0 ranges between 0.34 and 1.2 with a median value of 0.71. Farther away from emission sources, samples of BC particles were taken that were slightly older than those near the emission hot spot, but not yet embedded in liquid phase material. The 3D analysis gave $D_f = 1.9$ –2.6 with a median of 2.4, and $k_0 = 0.25$ –1.6 with a median 0.67. Thus aging of BC generally results in an observable increase of D_f .

The mean value of the monomer radius a typically varies in the size range from around 10 nm to 25 nm. For instance, in [51] the mean values of a for soot generated in turbulent diffusion flames was found to lie in the range 15–25 nm. In [52] diesel soot particles were found to have monomer radii in the range 14–17 nm, where the smaller monomers were generated at higher engine loads with higher operating temperatures. Other investigations on diesel soot found a mean monomer radius of 11 ± 3 nm [46]. Soot particles generated in the laboratory with a diffusion acetylene burner were found to have a mean monomer radius of 21 ± 4 nm [48]. Black Carbon collected in the field are composed of monomers of comparable sizes. For instance, a study in Mexico City as well as in a nearby area gave a monomer radius of 22 ± 6 nm [53]. In another field study [50] BC particles from two different sources yielded mean values of a of 26 nm and 18.5 nm; the monomers radii varied between 14–57 nm and 13–22 nm, respectively. The size of the monomer radius varies not only among aggregates, but even within each aggregate (e.g. [33,54–56]). Such polydisperse fractal aggregates can be seen in transmission electron microscope (TEM) images (e.g. [57]).

Inspection of TEM images further reveals that the aforementioned assumption of monomers in point contact is an idealisation (e.g. [58–60]). In reality, there is a finite contact surface between neighbouring spheres. Such morphological subtleties can be accounted for in models by allowing the spheres to overlap [60–64], or by adding material between neighbouring monomers, so-called necking [60,62,64–66]. Overlapping can be described by introducing an overlap factor [67]

$$C_{ov} = \frac{2a - d_{ij}}{2a}, \quad (4)$$

where d_{ij} denotes the distance between two neighbouring monomers. If that distance is equal to the monomer diameter $2a$, then $C_{ov} = 0$, i.e., the monomers are in point-contact. On the other hand, if $d_{ij} = 0$, then the spheres overlap completely, and $C_{ov} = 1$. Other authors [68] describe the degree of overlap by an overlap parameter

$$\delta = \frac{2a}{d_{ij}} = \frac{1}{1 - C_{ov}}. \quad (5)$$

Necking has been described, e.g., by adding material around the contact surface according to a three-dimensional Levelset function [60], or simply by linear or cylindrical connectors between neighbouring spheres [66].

Little quantitative information on overlapping or necking is available from measurements. Electron microscope analysis of wildfire smoke particles yielded $C_{ov} = 0.33$ [69]. Modelling studies assume either a fixed value of, e.g., $C_{ov} = 0.15$ [70], or they study the sensitivity to overlapping by considering a range of values, e.g., $C_{ov} = 0$ –0.33 [46], 0–0.4 [60], or 0–0.5 [68].

2.2. Morphology of coated black carbon particles

Diesel soot particles are often assumed to be emitted as pure BC, although small amounts of organic carbon (OC) have been observed in fresh diesel soot with BC/OC mass ratios ranging between 2 and 5 [71]. Biomass-burning aerosols originate from incomplete combustion of organic material, such as wood combustion [72] or wildfires [73,74], which typically produces brown carbon as well as BC coated with organic material. Also, aging of bare BC in the atmosphere is accompanied by oxidation of the particles, which increases their hygroscopicity (but it can also alter the dielectric properties of BC). Subsequent condensation of vapours onto the particles leads to internal mixing of BC with other components. Thus, aged BC, whether originating from diesel engines or biomass-burning, are often internally mixed with organic substances.

The condensation of sulphuric acid onto BC can accelerate the aging process [75]. Field-emission scanning electron microscope images reveal that BC particles mixed with small amounts of liquid-phase material can become coated by a thin film that fills out the void fraction in the aggregate [69]. On the other hand, heavily coated BC particles become partially or completely embedded in the liquid phase material. Depending on the amount and composition of the coating material, the coating can be spherical (e.g. [76]), or nonspherical (e.g. [53,69]). The most common coating materials are secondary organic compounds [13,53,77,78], sulphate [53,57,77,79], sulphuric acid [14], sea salt [57], and water [48,80–82].

Condensational growth of BC typically happens on a time scale of a few hours [83,84], which is short compared to the lifetime of anthropogenic aerosols in the atmosphere. For this reason, heavily coated BC particles are very common in the atmosphere. Correspondingly, the volume fraction of BC $f_{BC} = V_{BC}/V_{total}$, which expresses the ratio of the volume of black carbon to the total aerosol volume of an internally mixed aerosol, tends to fall off rapidly as the BC particles age and undergo condensational growth. For instance, two different studies of aircraft samples taken over and

near Mexico City showed median volume fractions of 15 % [77] and 7 % [53], respectively. Some of the samples were locally emitted, others originated from biomass burning sources outside the city. The Mexico city basin is rapidly ventilated with residence times typically less than 12 hours. It was estimated that most of the collected samples originating from local emissions had probably aged for about eight hours, while those from outside had aged for about 1–2 days [77]. This suggests that black carbon volume fractions larger than 15 % are likely to be limited to particles very close to emission sources.

Beside BC aggregates coated by or encapsulated in a shell of liquid material, some studies have considered BC aggregates attached to a sulphate sphere [85,86] or to a water droplet [81].

2.3. Size distribution

The median size of black carbon particles typically lies in the Aitken or accumulation mode, but it can vary significantly among samples. For instance, aircraft measurements of boreal biomass-burning aerosols in eastern/Atlantic Canada showed that aged particles lie predominantly in the accumulation mode with a median mobility-equivalent diameter of $D_m = 230$ nm and a modal width of $\sigma = 1.5$ [87]. Laboratory measurements found that the size distributions of freshly produced diesel soot as well as Palas soot peak at mobility-equivalent diameters around $D_m = 200$ nm; the size distributions of either type of black carbon evolves toward larger sizes over time as the particles interact dynamically and grow by coagulation [46].

Different measurement techniques have been used to study aerosol size distributions. The number size distribution can be obtained by use of a scanning mobility particle sizer (SMPS), differential mobility particle sizer (DMPS) [13], electrical low pressure impactor (ELPI) [88], electrical aerosol spectrometers [89], particle counters, such as passive cavity aerosol spectrometer probe [90], or analysis of scanning electron microscope (SEM) or transmission electron microscope (TEM) images [46,77,91]. The mass distribution of black carbon can be measured, e.g., by use of aerosol mass spectroscopy [92] or single particle soot photometers (SP2) [93].

SMPS and DMPS measurements yield the mobility-equivalent particle diameter, ELPI provides the aerodynamic diameter, while image analysis yields, e.g., the maximum dimension [46] or the size of a fitted ellipse [77]. Modelling studies often characterise the size of black carbon particles by specifying either the volume-equivalent radius r_v or the number and size distribution of monomers in the aggregate (as well as, if applicable, the overlap parameter or necking specifications). This can make it very difficult to precisely base model calculations on observations. However, some experimental studies have reported both the mean monomer radius a and the number of monomers N_s in the aggregate. These types of size measurements can more easily be used in modelling studies than, e.g., observations of aerodynamic or mobility-equivalent sizes. For instance, 3D TEM analysis of two different field samples produced mean values of $(a, N_s) = (26 \text{ nm}, 139)$ and $(18.5 \text{ nm}, 203)$ [50]. The number of monomers in the two samples varied in the range 7–509 and 47–792, respectively. The corresponding radii of gyration varied in the range 115–1017 nm and 99–560 nm, respectively. The same methodology applied to coated black carbon particles from a different sampling site gave mean values of $(a, N_s) = (22 \text{ nm}, 40)$ with a standard deviation of (6 nm, 32); the volume-equivalent radius of the host particle was 206 nm with a standard deviation of 71 nm [53]. Analysis of SEM images of soot particles freshly emitted from wildfires gave mean values of $(a, N_s) = (28 \text{ nm}, 498)$ and $(a, N_s) = (21 \text{ nm}, 437)$ with standard deviations of (6 nm, 995) and (5.5 nm, 846) [69].

2.4. Dielectric properties

Much of what we know about the dielectric properties of BC is inferred from laboratory studies, in which the soot particles are typically generated under controlled combustion conditions by use of pure fuels. BC in the atmosphere usually originates from diesel engines, coal combustion, or biomass burning under less ideal conditions. It is therefore not trivial to decide which laboratory studies provide results that can be generalised to atmospheric BC. A comprehensive review of the literature can be found in [94].

The most important microscopic properties that determine the dielectric properties are the electronic structure of the carbonaceous material, and the embedding of voids therein. Perfect lattice structures of carbon are diamond and graphite. The crystal lattice of diamond is built up of tetrahedral units of carbon atoms, in which the valence electrons are sp^3 hybridized (as in the methane molecule). This electronic structure is characterised by tightly bound electrons, resulting in low electric conductivity. By contrast, graphite is built up of unit cells in which the valence electrons of the carbon atom are sp^2 hybridized (as in benzene). These bonds are characterized by delocalised π electrons that can freely move along the lattice, resulting in high thermal and electrical conductivity. Correspondingly, diamond is optically transparent over a large spectral range from the UV to the far IR, while graphite is strongly absorbing.

Amorphous carbon can be seen as a mixture of sp^2 and sp^3 bonds [95]. While such a mixture does not display any large-scale order, it can have a characteristic structure on the scale of several atoms. This medium range order is one important factor that determines the dielectric properties of BC [96]. More specifically, the larger the graphitic clusters of sp^2 aromatic carbon rings, the lower the energy gap between the electronic ground state and the lowest excited state, resulting in enhanced absorption. The medium range order, in turn, depends on the combustion conditions.

Not only the electronic structure of BC, but also the content of voids entrained in the material during the formation process can impact the dielectric properties. Bond and Bergstrom [94] reviewed a sizable number of studies that inferred refractive indices from optical measurements at a wavelength of 0.55 μm . They investigated the variation of the imaginary part with the real part of the refractive index for the reported literature values and compared the results to theoretical predictions. They found that most of the reported values are consistent with the void fraction model, while a smaller number is consistent with the partial graphitisation model. Based on a discussion of the representativeness of available laboratory measurements for atmospheric BC, they conclude that the most realistic values for the refractive index should lie in the upper part of the void fraction curve. This range lies between $m = 1.75 + 0.63i$ and $1.95 + 0.79i$.

The spectral variation of the refractive index of flame soot has been studied in [97]. The spectral extinction measurements covered the wavelength range 0.20–6.4 μm . Calculations based on the subtractive Kramers–Kronig (SKK) technique [98] allowed for inferring the refractive index up to 30 μm wavelength. The following parameterisation was obtained as an empirical fit of the spectral dependence of the real part n and the imaginary part k of the refractive index.

$$n = 1.811 + 0.1263 \ln \lambda + 0.027 \ln^2 \lambda + 0.0417 \ln^3 \lambda \quad (6)$$

$$k = 0.5821 + 0.1213 \ln \lambda + 0.2309 \ln^2 \lambda - 0.01 \ln^3 \lambda, \quad (7)$$

where the wavelength λ is given in μm . The parameterisation is accurate in the wavelength range 0.4–30 μm . For shorter wavelengths, the authors reported $m = n + ik = 0.94 + 0.35i$ at $\lambda = 0.20 \mu\text{m}$, and $m = 1.19 + 0.79i$ at $\lambda = 0.26 \mu\text{m}$, where both values are based on measurements 10 mm above the burner surface

of a propane flame. At 0.55 μm wavelength, the parameterisation yields $m = 1.74 + 0.59i$, while the measurements at 0.54 μm gave $m = 1.77 + 0.63i$. Both values lie along the upper part of Bond and Bergstrom's void fraction curve [94].

In light scattering modelling of soot at and near a wavelength of 0.55 μm it has become popular to use the value of $m = 1.95 + 0.79i$ (e.g. [86,99]), but lower values along the void fraction curve are also being used, such as $m = 1.75 + 0.63i$ (e.g. [100,101]). When a spectral variation is considered, one frequently uses the parameterisation determined in [97] and given here in Eqs. (6) and (7) (e.g. [7,100,102]), which has the advantage of covering a large spectral range.

However, owing to the high variability in the degree of graphitisation and in the amount of void fractions in the material, the refractive index of soot can vary considerably. Therefore it is imperative to consider this variability as an important source of model uncertainty. This has been discussed in [103], in which the refractive index was parameterised according to

$$n = n_0 + A(\lambda - 0.55) \quad (8)$$

$$k = k_0 \cdot 10^{B(\lambda - 0.55)}. \quad (9)$$

Here $n_0 + ik_0$ denotes the refractive index at a wavelength of $\lambda = 0.55\mu\text{m}$. Note that the parameterisation is limited to the spectral range of 0.3–1.0 μm . The authors fitted the parameterisation to different measurements reported in the literature [13,34,97,104–106]. They concluded that the uncertainty range of the refractive index of soot is well represented when varying the fitting parameters in the ranges $0.0 \leq A \leq 0.25$ and $-0.25 \leq B \leq 0.0$, although some observations lie even outside this range. The reference value $n_0 + ik_0$ varies among different studies within a range similar to that given in [94].

3. Computational methods

Numerical methods for light scattering computations are typically much simpler for regularly shaped particles (e.g. [107,108]), than for irregular particles, such as soot. Both approximate and numerically exact methods have been employed for modelling optical properties of BC aggregates. The Rayleigh–Debye–Gans (RDG) theory ([25,109]) is perhaps the most widely used approximate method (e.g. [110–113]). For instance, it is the basis of the COSIMA computer program for simulating the dynamics of fractal BC aggregates [114]. It has also been applied to the retrieval of soot properties from light scattering measurements (e.g. [115]). The first assumption in RDG theory is that the monomer radius a is small compared to the wavelength λ ,

$$2\pi a/\lambda \ll 1. \quad (10)$$

Thus each monomer scatters in the Rayleigh limit. The second assumption is that the monomers are optically soft, i.e.

$$|m - 1| \ll 1, \quad (11)$$

where m denotes the refractive index of the monomers. Under the second assumption multiple electromagnetic interactions among the monomers are negligibly small, and each monomer can be assumed to only interact with the incident electromagnetic field. While the first assumption is often well satisfied for BC aggregates, the second one is not [113]. For this reason, several studies have evaluated the range of validity of the RDG approximation (e.g. [116]). Such evaluations are based on comparing RDG results to either numerically exact results [113,117,118], or to measurements on aggregates of TiO_2 and SiO_2 [119] as well as BC [120].

Among the earliest work on accounting for electromagnetic interaction among monomers were studies based on the method

of moments [121,122] and the coupled dipole method [122,123], where each monomer is treated as an electric dipole. Extensions of RDG theory have been developed, e.g., by introducing corrections for multiple scattering among monomers [124,125]. Karlsson et al. introduced a generalised RDG theory based on accounting for the electric near-field interaction among monomers, while neglecting electric far-field interaction [126,127]. Other approximate methods have been devised, such as the grouping adding method [128], an electrostatic approximation method [129], and the geometric-optics surface-wave approach [130].

With the steady advance of computational capacities numerically exact methods have become increasingly popular. The Multipole sphere T matrix (MSTM) method is based on using the superposition formulation for radiative interactions among monomers [131–133]. A publicly available superposition T matrix code has been developed [134] which makes use of analytic orientation averaging for randomly oriented particles [135,136]. An updated version of the MSTM code has been tailored to parallel computing environments [137]. The monomers in the aggregate can be located either internally or externally to each other, and they can have different dielectric properties. There are only two restrictions. (i) All monomers must be homogeneous spheres. (ii) The monomers must not intersect each other; i.e., the surfaces of any two spheres, whether internal or external to each other, must have, at most, a single point of contact. A main strength of the method is its high computational speed and accuracy in comparison to other numerically exact methods. The MSTM code has been employed extensively in applications to BC aggregates (e.g. [55,81,85,86,117,138–148]).

An equally popular numerically exact approach is the discrete dipole approximation (DDA), which was originally developed by Purcell and Pennypacker [149]. Reviews of the method can be found, e.g., in [122,150]. Publicly available computer implementations are DDSCAT [151] and ADDA [152]. The method has no restrictions on particle shape; it can accommodate, e.g., overlapping spheres, necking, and nonspherical monomers. However, it is slower than the MSTM; orientation-averaging is carried out numerically rather than analytically. A sizable number of modelling studies on BC is based on using the DDA (e.g. [60–62,64,66,101,102,118,144,153–161]).

An important issue in application of the DDA is the choice of the dipole spacing d , which controls the accuracy of the results (e.g. [162]). The quantity $|m|kd$, where m is the complex refractive index, and k is the wavenumber in vacuum, has to be chosen sufficiently small so that (i) the dipole approximation holds (e.g. [29,163]); and (ii) the geometry of the particle is sufficiently well approximated by the array of dipoles (e.g. [163]). The best choice of $|m|kd$ depends on the optical properties of interest. Differential scattering properties typically require a smaller dipole spacing than integral optical properties. It may also depend on the specific geometry, and on whether or not the aggregates are coated. But in general, the dipole spacing for BC aggregates has to be chosen much smaller than for compact particles (e.g. [155,163]). One can investigate the accuracy of the DDA results by checking the convergence with decreasing d (e.g. [164,165]), by comparison with T-matrix results (e.g. [155,163]), or, possibly, by use of the reciprocity condition [166]. A systematic study of the performance of the DDA for computing optical properties of BC aggregates has been reported in [163].

Another efficient method for aggregates of non-overlapping spheres is the Generalised Multiparticle Mie method (GMM) [167–170], which has been applied to BC aggregates in [140]. In the latter paper, the GMM was also compared to the MSTM. The otherwise popular Finite-Difference Time-Domain method (e.g. [171]) is only occasionally applied to BC aggregates (e.g. [161]). A finite element method, referred to as the finite-element boundary integral

domain decomposition method, has been presented and applied to randomly oriented aggregates, as well as compared to MSTM results [172]. A machine learning method to estimate integral optical properties of soot has been reported in [146]. The authors employed a supervised learning model that has been trained with data generated by use of the MSTM code.

Comparison of the RDG and MSTM applied to BC can be found in [117,173]. Comparisons of DDA and MSTM applied to BC have been presented in [144,155,163]. The geometric-optics surface-wave approach has been compared to MSTM computations for BC aggregates in [99].

4. Optical properties of pure black carbon aggregates

RDG theory can, in some cases, provide sufficiently accurate predictions of the absorption cross section of pure BC aggregates, while in other cases, it can under-predict absorption by 10–20 % (e.g. [174]). This has spawned the development and use of numerically exact methods for modelling optical properties of pure BC aggregates. In [138] it was shown that accounting for electromagnetic interaction among monomers in BC aggregates enhances absorption by more than 25 %, while the single scattering albedo (SSA) and the asymmetry parameter g can be enhanced by more than a factor of 10. The phase function acquires a pronounced forward peak as compared to the Rayleigh-like phase function of independently scattering small monomers. A comprehensive sensitivity study of the integral optical properties to changes in D_f for a selection of different values of k_0 , a , N_s , and refractive index m has been reported in [139]. One of the refractive indexes as well as about half of the range of fractal dimensions considered in that study were representative for atmospheric BC aerosols. It was found, in most cases, that the optical cross sections and the asymmetry parameter increase monotonically with increasing D_f . However, for large lacy aggregates one can observe an initial decrease of the absorption cross section as the aggregates becomes more compact, followed by a monotonic increase at higher values of D_f . These findings underscore the importance of accounting for electromagnetic interaction among monomers in modelling the integral optical properties of BC aggregates.

The work reported in [140] included a comparison between MSTM and GMM computations for bare, monodisperse BC aggregates. The GMM method allows for approximate solutions based on introducing an interaction index $f_{i,j} = (a_i + a_j)/|\mathbf{r}_i - \mathbf{r}_j|$, where a_i and a_j are the radii of monomers i and j , and $|\mathbf{r}_i - \mathbf{r}_j|$ is the separation of their centres of mass. Interaction among all monomers with an interaction index $f_{i,j}$ smaller than a prescribed value f_0 is neglected. The exact solution corresponds to $f_0 = 0$, and the RDG solution to $f_0 = 1$. The method is able to interpolate between those, which gives us an idea of how important and how far-reaching electromagnetic interaction among monomers within an aggregate is. The computations were performed for aggregates in the range from $N_s = 5$ up to $N_s = 1000$, and for $D_f = 1.82$, $k_0 = 1.27$. The results revealed that the approximate solution only gave good agreement with the exact solution for both the cross sections and the asymmetry parameter if $f_0 \leq 0.02$. This strongly suggests that electromagnetic interactions among monomers can be far-reaching, even in such relatively lacy aggregates. The study further investigated the sensitivity of the integral optical properties to a variation in m and a . The parameter range was limited to values representative of atmospheric BC. It was found that the mass absorption cross section (MAC) monotonically increased as the refractive index was varied from $1.75+0.63i$ to $1.95+0.79i$. The SSA only changed from 0.22 to 0.26. By contrast, an increase in a from 15 to 25 nm resulted in no change in MAC, and in a monotonic increase in SSA from 0.18 to 0.26. It was concluded that MAC is highly sensitive to

a variation in the refractive index, while an increase in monomer radius mainly increases the single scattering albedo.

Polydispersity of aggregates can impact the optical properties [54]. For instance, in [63] total cross sections as well as differential scattering cross sections were compared for (i) monodisperse aggregates with a monomer diameter $2a = 34$ nm, and (ii) polydisperse aggregates with a mean monomer diameter $2\bar{a}=34$ nm and a standard deviation $\sigma = 6.9$ nm, where the size distribution was assumed to be Gaussian. They found that polydispersity enhanced the cross sections. Similar findings were reported in [55], in which a larger number of samples was used for computing ensemble-averaged optical properties. A lognormal size distribution for the monomers was assumed:

$$n(a) = \frac{1}{a\sqrt{2\pi} \ln \sigma} \exp \left[-\left(\frac{\ln(a/a_0)}{\sqrt{2} \ln \sigma} \right)^2 \right]. \quad (12)$$

The optical cross sections and the asymmetry parameter obtained for polydisperse aggregates were compared to those of monodisperse aggregates, where the latter were computed for monomer radii $a = a_0$, and a_0 denotes the geometric mean radius of the log-normal distribution. As in [63], the monodisperse aggregate model tends to give lower cross sections than the polydisperse model. However, the authors also tested a different measure of equivalent monomer radius a_{vol} defined such that a monodisperse aggregate composed of N_s monomers of radius a_{vol} has the same volume as a corresponding polydisperse aggregate of N_s monomers, i.e.

$$N_s \frac{4\pi a_{\text{vol}}^3}{3} = N_s \int \frac{4\pi a^3}{3} n(a) da. \quad (13)$$

Monodisperse aggregates with this equivalent monomer radius gave much better agreement with the polydisperse aggregates, but they still underestimated the scattering cross section by 10 %. Similarly, a volume-equivalent monomer diameter was defined in [143] according to

$$d_v = \sqrt[3]{\sum_{i=1}^N d_i^3 / N}, \quad (14)$$

where d_i denotes the diameter of the i th monomer. Computations of optical properties of volume-equivalent aggregates showed that in most cases the cross sections and SSA were similar when comparing polydisperse aggregates with monodisperse aggregates composed of monomers with diameter d_v . However, the differences were larger for more extreme cases of polydispersity.

The existing literature on polydispersity gives little clues as to why one should choose one measure of size equivalence or the other. Neither the use of a geometric mean radius a_0 nor the use of an equivalent volume radius a_{vol} seems to be based on any assumptions grounded in the relevant physical processes, namely, the interaction of light with aggregated particles. If the monomers were independent scatterers, they would be in the Rayleigh regime. Also, it is known that the absorption cross section of monodisperse BC aggregates scales with the volume of the particles (e.g. [7]), i.e. $C_{\text{abs}} \propto Na^3$, just as in Rayleigh scattering. For this reason, a physically well-motivated measure of monomer size-equivalence could be obtained by averaging a over the size distribution weighted by the particle volume; i.e., we could define an effective monomer radius by

$$a_{\text{eff}} = \frac{\int \frac{4}{3}\pi a^3 n(a) da}{\int \frac{4}{3}\pi a^3 n(a) da}, \quad (15)$$

which is the ratio of the fourth to the third moment of the size distribution. Note the analogy to the definition of the effective radius of particles in the geometric optics regime as the ratio of the third to the second moment of the size distribution (since in that

regime, the optical cross sections scale with the cross sectional geometric area of the particles). Clearly, a_{eff} is shifted to larger radii compared to a_0 , which explains why monodisperse aggregates with a radius a_0 underestimate the optical cross sections, especially C_{abs} . It remains to be seen how such a measure of size equivalence would perform in practice. Note that other optical properties of aggregates do not display a simple scaling relation with the particle volume [7]. Therefore, it is by no means guaranteed that assuming a measure of size equivalence grounded in optical scaling relations will automatically give us a better representation of the optical properties of polydisperse aggregates. But in general, it still seems most promising to base a size-equivalence measure on our understanding of optical processes. An indirect clue may come from the sensitivity study of SSA as a function of a reported in [140]. It was found that modelled SSA values gave the best agreement with reported measurements (reviewed in [94]) for $a = 25$ nm, which lies close to the upper end of monomer radii found in measurements (also reviewed in [94]). For smaller monomer radii, SSA was too low, because the scattering cross section C_{sca} was too low. It is quite possible that the size measure a_{vol} used by [55] underestimates C_{sca} , because it is only based on the third moment of the size distribution, which gives too low values for the effective monomer radius. A physically motivated size measure based on the fourth moment of the size distribution, such as in Eq. (15), would be shifted to larger radii, resulting in higher values of C_{sca} .

The effect of monomer shape has been investigated in [158]. Aggregates composed of spherical monomers were compared to those composed of axis-parallel spheroidal monomers, where the spheroidal monomers had the same volume as the spherical ones. The simulations were performed for a range of different fractal dimensions, monomer radii, wavelengths, refractive indices, and spheroid aspect ratios R_a/R_b , where R_a and R_b denote the dimension perpendicular and parallel to the spheroid's symmetry axis, respectively. The authors concluded that monomer shape has a large impact on optical properties; nonsphericity enhances C_{abs} by up to 15 %, SSA by up to 10 %, and it reduces the asymmetry parameter g by as much as -25 %. However, upon closer inspection of these results one should note that the maximum variation given in this summary correspond to rather extreme monomer shapes. The aspect ratio of the spheroids was varied between 1/3 and 3, and all spheroidal monomers had the same orientation. This results in aggregate morphologies that are, arguably, not very realistic. Further, some of the diagrams in the paper by [158] show that the fractal dimension and the refractive index of soot have a stronger impact on MAC and SSA than the monomer nonsphericity. The monomer radius a has a profound impact on SSA, which confirms the results reported in [140]; this impact far exceeds that of the monomers' aspect ratio.

Deviations from the idealised assumption of point-contacting monomers have been discussed extensively in the literature [60,61,63–66,68]. Both overlapping and necking was systematically studied for a bisphere in [66]. It was found that different necking models do not lead to significant differences in the optical properties. Therefore, the authors recommend to use the simple cylindrical connector model. An increase in the overlap factor C_{ov} between 0 and 0.18 results in a monotonic increase of C_{abs} by about 4 %, followed by a monotonic decrease. Between $C_{\text{ov}} = 0.18$ and 1 the absorption cross section drops by about -8 %. A comparison of fractal BC aggregates of three different sizes showed that 20 % overlapping of the monomers slightly decreased C_{abs} as compared to point-contacting aggregates, and it increased C_{sca} [63]. A systematic study for a range of different overlapping and necking parameters on realistic, polydisperse BC aggregates was presented in [60]. The study covered the spectral range from 266 to 1064 nm. It was found that the mass extinction cross section,

C_{ext}/m_p (where m_p denotes the particle mass), is lowered by overlapping and necking in the UV, and enhanced in the visible and near IR part of the spectrum. The asymmetry parameter is lowered over the whole spectral range, while SSA is enhanced for all wavelengths. The magnitude of the impact on extinction and SSA is largest for shorter wavelengths.

Thanks to a substantial amount of work invested into optical modelling, we have now reached a fairly high level of understanding of how various morphological properties impact the integral optical properties of bare BC aggregates. It is clear that there are substantial differences in the optical properties of fractal aggregates and mass-equivalent spheres. For instance, a fractal aggregate model of BC can yield spectral [18] and broadband [7] radiative forcing estimates that are higher by a factor of 2 than corresponding estimates based on a homogeneous sphere model. Part of the problem is that the homogeneous sphere model underestimates C_{abs} , and it overestimates SSA. This gives too little radiative warming by absorption and too much radiative cooling by scattering. These two errors are additive in radiative transfer simulations. The poor performance of homogeneous spheres in representing absorption by soot can be understood physically [8]. A compact sphere of highly absorbing material shields part of the BC mass near its centre from interacting with the electromagnetic field. By contrast, a lacy aggregate allows a larger part of the BC mass to come into contact with the field, thus contributing to absorption of radiative energy. This is why the homogeneous sphere model underestimates C_{abs} .

By contrast, comparing fractal aggregate models with fractal parameters $(D_f, k_0) = (2.4, 0.7)$ and $(1.8, 1.3)$ only leads to differences in the broadband radiative forcing by a factor of 1.1–1.6 [8]. More subtle morphological features can be expected to have an even smaller impact. Therefore, based on our current state of knowledge, it seems most reasonable that pure BC aerosols should be represented in models by monodisperse, point-contacting, spherical monomers (with a suitable measure of size-equivalence for the monomer radius). Minor morphological features should be accounted for by including them in the error estimates, or by employing a simple empirical correction. An important step toward such an approach was made in a recent study [64]. The authors quantified the effect of five minor morphological structures, namely, monomers with polydispersity, irregular shapes, and thin coatings, as well as necking and overlapping. It was found that these minor structures only have a small effect on the asymmetry parameter and on the elements of the Mueller matrix. The effect on the scattering and absorption cross section is more significant, but much of this can be attributed to the effect of minor structures on the particle volume. Necking has the strongest effect. In the Rayleigh regime, $C_{\text{abs}} \propto V$ and $C_{\text{sca}} \propto V^2$, where V denotes the particle volume. Thus it was proposed to introduce empirical correction factors B_{abs} and B_{sca} and to make the ansatz

$$C_{\text{abs}} = B_{\text{abs}} \frac{V}{V_0} C_{\text{abs}}^0 \quad (16)$$

$$C_{\text{sca}} = B_{\text{sca}} \left(\frac{V}{V_0} \right)^2 C_{\text{sca}}^0, \quad (17)$$

where C_{abs} , C_{sca} , and V denote the cross sections and particle volume in the presence of minor structures, while C_{abs}^0 , C_{sca}^0 , and V_0 denote the corresponding quantities for the idealised monodisperse, bare aggregates of homogeneous spheres in point-contact. At a wavelength of 500 nm, it was found that a correction factor of $B_{\text{abs}} = B_{\text{sca}} = 1.05$ resulted in very good agreement with numerically exact reference computations accounting for aggregates with non-ideal minor structures. Thus, when the effect of minor structures on the particle volume is accounted for, the remaining

effect of these morphological features on the optical cross sections is remarkably small; it is only on the order of 5 %.

For fractal aggregates consisting of monodisperse, point-contacting spherical monomers a data base of optical properties has been described in [148]. The authors of that study make the data base available upon request.

Linearly polarised light becomes partially depolarised upon scattering by BC aggregates [175]. It is evident that depolarisation is caused by electromagnetic interaction among the monomers in the aggregate, as non-interacting monomers would not change the polarisation state. The sensitivity of depolarisation to morphological properties was tested [65] by use of DDA computations. The DDA was also compared to a simplified model that limits multiple scattering among monomers to second order. The approximate model was found to be overall consistent with the DDA results. The simulated backscatter depolarisation ratio δ_l decreases with increasing D_f , it increases with N_s for $N_s \geq 20$, and it increases with monomer radius a . δ_l was also found to increase with $|m|$. However, m was varied from $1.16+0.71i$ to $2.65+1.32i$, resulting in a variation of δ_l from 0.0025 to 0.025. Only a small sub-interval of these values of m are representative for atmospheric BC. Within that sub-range the variation of δ_l is very small. Overlapping and necking can enhance δ_l from 0–0.005 for point-contacting spheres to 0.005–0.03 for aggregates with strong overlap/necking. For sufficiently large values of N_s , δ_l depends most strongly on a . However, in most cases typical for atmospheric BC the depolarisation ratio of bare BC aggregates rarely exceeds 0.01–0.03.

In [176] the extinction and backscattering cross section, the lidar ratio LR , and the linear depolarisation ratio δ_l in the backscatter direction were simulated for bare BC aggregates. A sensitivity analysis suggested that (i) all of these lidar-relevant quantities are sensitive to the monomer radius; (ii) the number of monomers had a strong impact on the cross sections (as expected), but not so much on δ_l ; and (iii) the fractal dimension of the aggregates only had a weak impact on all lidar-relevant optical properties.

5. Optical properties of black carbon aggregates mixed with liquid material

The simplest model to describe BC mixed with liquid material is to assume a homogeneous sphere, and to compute an effective refractive index of the BC/liquid mixture by use of effective medium theory (EMT) (e.g. [177,178]), such as the Maxwell-Garnett [179] or the Bruggemann rule [180]. Since the mixing with BC “darkens” the liquid material, we will refer to this as the homogeneous grey-sphere model. Only if the size parameter $x = 2\pi R/\lambda$ of the BC inclusions is smaller than 0.5, where R is the radius of a volume-equivalent sphere, then EMT reproduces the integral optical properties with 1 % accuracy [181]. For instance, for a monomer radius of $a = 25$ nm and $\lambda = 500$ nm, this would correspond to a fractal aggregate composed of less 17 monomers. Comparisons with detailed DDA computations showed that, in general, EMT models tend to underestimate the scattering efficiency and overestimate the asymmetry parameter and absorption efficiency [156,182].

Among the earliest inhomogeneous particle models were the concentric [183] and non-concentric spherical core-shell models [184,185], in which the liquid-phase material makes up the shell, and BC makes up the core. Another approach is the equivalent coated sphere model, in which the shell has the index of refraction of the aggregate, and the core has the index of refraction of the surrounding medium [186,187]. Slightly more complexity is added in the spherical concentric core-shell dimer model [188]. An extension of this model is the so-called closed cell model, in which the aggregate is composed of core-shell monomers. The BC monomers are concentrically [35,80,130,189–193] or off-centre coated [194], and the shells of the monomers are in point contact with neigh-

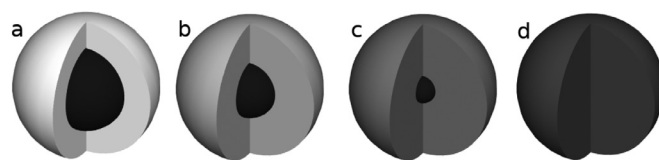


Fig. 2. Core-grey-shell (CGS) model with variable choices of the free tuning parameter, i.e., the BC core fraction f_{core} . Limiting cases comprised by the CGS model are the core-shell model (a) with $f_{\text{core}} = 1$, and the homogeneous grey-sphere model (d) with $f_{\text{core}} = 0$.

bouring core-shell monomers. It was shown that this model approximates the optical properties of more realistic BC monomers in point contact coated with a film of weakly absorbing coating material if the BC volume fraction is higher than 0.75. For thickly coated aggregates, a model consisting of a spherical shell with multiple spherical BC inclusions has been considered [153]. Shortly after that the first models of morphologically realistic fractal BC aggregates encapsulated in a shell of homogeneous [155] and inhomogeneous liquid materials [53] have been considered. Comparisons of morphologically realistic and more or less simplified morphologies are reported in [148,153,155,156,190].

From a climate modelling perspective, one of the main concerns is the question by how much the coating enhances light absorption compared to bare BC aggregates (e.g. [195]). A significant number of studies have investigated this problem by use of modern coated aggregate models. For instance, computations for fractal BC aggregates encapsulated in a spherical shell of sulphate were compared to three simplified model particles [155]. The simplest one of those was an external-mixture model, in which BC and sulphate each are described by separate homogeneous spheres of equivalent volume. Calculations were reported for one UV, one visible, and one NIR wavelength. The use of the external-mixture model results in substantial biases in the optical cross sections. Depending on particle size, wavelength, and BC volume fraction, C_{abs} of coated fractal aggregates can be 3–8 times higher than the corresponding averaged absorption cross section in the simple external-mixture model. In the same study, the encapsulated aggregate model was compared to a homogeneous grey-sphere model based on using EMT according to Maxwell-Garnett [179]. It was found that the homogeneous-mixture model generally overestimates absorption. Finally, the concentric core-shell model was shown to underestimate absorption at the visible and the NIR wavelength (see Figs. 5–8 in that paper), but generally not at the UV wavelength (Figs. 2 and 3). Similar results were later reported in [191]. These results were further corroborated in a more comprehensive study covering the entire spectral range from 230 nm to 8.0 μm [156]. The biases introduced by the external-mixture, EMT, and core-shell models were most pronounced in the visible and near IR part of the spectrum, where most of the solar energy is found. It was also shown that the overestimation of C_{abs} by the core-shell model extends over the entire visible spectrum and into the NIR (see Fig. 4 in that paper). Thus, despite a possible overestimation at wavelengths below 350 nm [155,191], the core-shell model will overestimate broadband absorption by coated BC aerosols.

Another investigation with a focus on BC aggregates covered with sea salt compared coated with uncoated aggregates [157]. Averaged over the spectral range from 200 to 1000 nm, the coating enhanced MAC by a factor ranging between 1.0 for lacy, partially immersed BC aggregates, up to 2.2 for compact, fully encapsulated aggregates. Similar results were reported in [101]; they considered sulphate-coated BC aggregates with various fractal dimensions and BC volume fractions, but for a single wavelength of 550 nm. It was shown that for a BC volume fraction of 0.15, coating enhances absorption of bare BC aggregates by a factor ranging from 1.5 to 1.65,

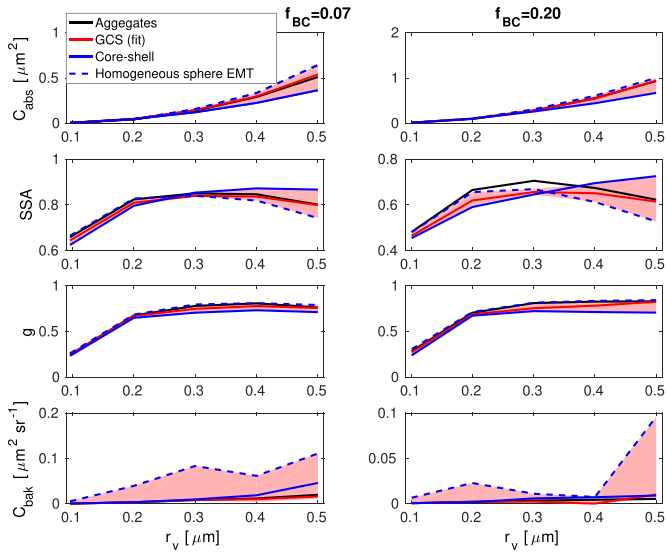


Fig. 3. C_{abs} (top row), SSA (second row), g (third row), and C_{bak} (bottom row) as a function of volume-equivalent radius r_v obtained for BC volume fractions of $f_{\text{BC}} = 0.07$ (left column) and 0.20 (right column) at a wavelength of $\lambda = 533$ nm. Results are obtained for a sulphate-coated fractal aggregate model (black), CGS model with $f_{\text{core}} = 0.5$ (red), core-shell model (solid blue), and homogeneous grey-sphere model (dashed blue). The range of CGS results with different choices of f_{core} is indicated by the shaded region. (For interpretation of the references to color in this figure legend, the reader is referred to the web version of this article.)

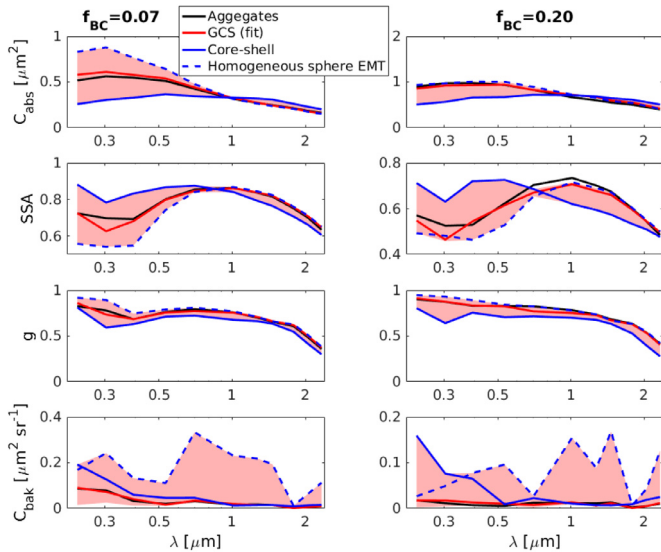


Fig. 4. As Fig. 3, but for a fixed particle radius $r_v = 500$ nm. Each optical property is shown as a function of wavelength (note the logarithmic scale).

where the higher end corresponds to aggregates with larger fractal dimension.

The work in [62] examined coated BC aggregates in the spectral range of 266–1064 nm. The coating was non-spherical and more or less followed the shape of the aggregate. For the aggregates, the effects of monomer polydispersity, overlapping and necking have been taken into account, and the sizes ranged from $N_s = 1$ –96 monomers. The absorption enhancement factor varies between 1 and 1.5, depending on the coating thickness. The core-shell model was shown to overestimate the enhancement factor, while a model based on individually coated monomers strongly underestimates the absorption enhancement.

A model with a focus on BC aggregates coated with a thin film of organic material (with a BC volume fraction of 0.8) reported an

absorption enhancement factor of 1.15 [160]. The calculations were limited to a wavelength of 550 nm. This relatively small absorption enhancement for weakly coated particles would be more typical for freshly emitted BC aerosols. Field measurements from both winter and summer campaigns in near-source environments confirm that absorption enhancement of such BC particles is rather small [196].

A study focusing on coated BC particles at wavelengths 532 nm and 1064 nm reported computations with the MSTM model for BC mass fractions in the range 0.01–1 [147]. The mass fraction is defined analogously to the volume fraction, i.e., $f_{\text{BC}}^m = M_{\text{BC}}/M_{\text{total}}$, where M_{BC} and M_{total} denote the masses of the BC aggregate and of the total BC+coating particle, respectively. It was shown that the absorption enhancement factor increases with decreasing BC mass fraction; it reaches a constant average value of 2.5 at mass fractions $f_{\text{BC}}^m \leq 0.01$. Another MSTM study limited to computations at a wavelength of 550 nm and to BC aggregates fully encapsulated in a spherical sulphate shell reported absorption enhancement factors in the range between 1.3 and 2.4 varying with BC volume fraction, off-center position of the BC core, fractal prefactor, and size class [145].

Scaling relations of the MAC enhancement factor E_{MAC} were reported in [197]. The study compared measurements with a coated aggregate model for BC mass fractions $f_{\text{BC}}^m = 0.07$ –1.0 and for wavelengths 405, 532, and 880 nm. It was found that the wavelength dependence of MAC follows a λ^{-1} power law. More specifically, MAC of the coated BC aggregates can be described by $\text{MAC} = 3.6 f_{\text{BC}}^{m-1/3} \lambda^{-1}$. Note, however, that the refractive index of BC as well as the coating was assumed to be independent of wavelength in that study. They further found that the absorption enhancement factor due to the coating ranged between 1.3 and 1.9 for partially embedded BC, and between 2.2 and 2.5 for BC that is completely encapsulated by the coating. The enhancement factor E_{MAC} can be modelled as $E_{\text{MAC}} = 1.0 f_{\text{BC}}^{m-0.32}$.

The spectral variation of the optical properties, and specifically the extinction Ångström exponent (EAE) and absorption Ångström exponent (AAE) were investigated in several studies [103,156,191,192,198]. The spectral ranges considered were 230 nm–8.0 μm [156], 350–880 nm [198], 355–1064 nm [191], 300–1000 nm [103], and 350–700 nm [192]. The optical cross sections, EAE, and AAE depend on particle size and spectral range [156], on the assumed particle morphology [191], as well as on BC volume fraction, to whether the coating material is absorbing or not, and to the fractal dimension D_f [192]. In general, the Ångström exponents are more sensitive to particle morphology at lower wavelengths, where the size parameter is higher [198]. The modelling results demonstrate that AAE can be significantly different from unity [103,198], while it has previously been assumed that $\text{AAE} = 1.0$ is a reasonably good approximation, at least for BC emitted from motor vehicles (e.g. [106]).

Other studies considered more subtle morphological features. The effect of polydispersity on the optical properties of coated BC aggregates was studied in [143]. It was found that polydispersity enhances the single scattering albedo by up to 50 %, while the effect on C_{abs} is less than 8 %. It has been shown in [140] for monodisperse aggregates that the SSA is mainly sensitive to the size of the monomers, while the optical cross sections are not strongly affected by the monomer size. This indicates that the large discrepancy in SSA between the polydisperse and monodisperse model reported in [143] may be caused by the use of an inadequate measure of monomer size equivalence. In fact, the comparison in [143] was based on defining the equivalent monomer size of monodisperse aggregates as in Eq. (14). This definition of size equivalence is certainly more adequate than to simply use the mode radius of the lognormal monomer size distribution. However, as argued in Section 4, an even more suitable, and physically better

motivated measure of size equivalence may be the one proposed in Eq. (15). This hypothesis remains to be tested.

Whenever aggregates become only partially embedded in the liquid phase coating, part of the aggregate sticks out of the coating [144]. As a result, some of the monomer surfaces may intersect with the surface of the coating. The MSTM cannot be applied to such geometries. One has to resort to using the numerically more demanding DDA. Two different approaches have been proposed for constructing partially embedded soot aggregates with the additional constraint that the surfaces of the monomers and the coating do not intersect. In one model [144], the first two monomers are placed on either side of the coating, i.e., one on the inside and the other on the outside, such that the two monomers and the coating all touch in a single common point. Subsequently, more monomers are added to the outside and inside so that the fractal scaling relation in Eq. (1) is satisfied in each step of the construction process. The total number of monomers and the size of the monomers and coating (thus the volume fraction), as well as the number of inside and outside monomers are prescribed. In another model [199], the aggregates are first formed and placed inside the coating with a prescribed displacement of the centres of mass. Subsequently, all overlapping monomers are displaced by a small distance outward until they no longer overlap with the coating. The approach proposed in [144] has the advantage that the model particles have well defined fractal parameter D_f and k_0 . It is unclear to what extent the displacement of monomers in [199] may alter the fractal parameters of the particles. In either case, elimination of the problem of overlapping spheres allows us to use of the MSTM. In [144] MSTM results were compared to corresponding DDA computations for particles that had the exact same fractal parameters, and in which the same fraction of the aggregate protruded out of the coating, but the particles were constructed without the constraint of non-intersecting surfaces. It was found that differences in C_{sca} , SSA, and g were less than 1 %, while C_{abs} differed by less than 5 %. These findings are of great practical value, as they suggest that integral optical properties can be computed by the MSTM by use of the non-intersecting sphere model proposed in [144], as long as all monomers as well as the coating are spherical.

The positioning of the BC core inside the liquid phase host particle has been considered by several authors [53,155,156,188,191]. In general, BC cores that are placed off-centre have lower absorption cross sections than corresponding model particles in which the centres of mass of the BC core and the coating coincide. However, the magnitude of this effect can vary. In [188] a spherical core-shell model has been employed. The size of the spherical BC core was fixed at $a = 10$ nm, while the total size of the composite particle was varied between 0.01 and 1 μm . Concentric core-shell particles were compared to one model with randomly placed inclusions, and to another model with subsurface inclusions. The MAC results did not differ appreciably up to particle sizes of 0.15–0.2 μm , beyond which they started diverging. The concentric core-shell particles displayed, on average, the highest MAC values, while the particles with subsurface BC inclusions lay lowest. However, it was estimated that concentric core-shell geometries will overestimate absorption by no more than 15 %. The spherical concentric and eccentric core-shell model was recently revisited for fixed BC volume fractions of $f_{BC} = 0.07$ and 0.15 [191]. The results largely confirmed those found earlier in [188]. For instance, for $f_{BC} = 0.07$, a core radius of 0.1 μm , a composite particle radius of 0.243 μm , and at a wavelength of 532 nm, the absorption cross section modelled with the concentric core-shell model lies about 8 % higher than that obtained with a subsurface spherical core shell model. Computations with a more advanced embedded fractal aggregate model showed that moving the BC aggregate off the centre can reduce absorption by up to 20–30 % [53].

The fact that the concentric spherical core-shell model predicts higher absorption than the corresponding eccentric core-shell model seems to be more of a side-issue, considering that, on the whole, that model was shown to strongly underestimate absorption in comparison to more realistic coated aggregate models [155,156]. By moving the core off the centre, this problem only increases. The remedy is the so-called core grey shell model [156], which will be discussed in Section 7.

The chemical composition, and thus the refractive index of the coating is another important aspect that has been discussed in several papers [188,191,192,200]. The sensitivity of the Ångström exponent and the linear depolarisation ratio on the refractive index is particularly pronounced. It may even be strong enough to allow us to obtain information about the composition of the coating from measurements of the Ångström exponent and of δ_l [200].

To understand the relation between morphology and the linear depolarisation ratio δ_l is among the most challenging and interesting topics in aerosol optics. One of the earliest studies based on the use of a realistic encapsulated aggregate model assumed that the BC core is off-centre, partially sticking out of the coating, and that the shell has spherical shape. Results for the full Mueller matrix have been reported at a wavelength of 533 nm for particles with a volume equivalent radius of 0.5 μm and a BC volume fraction of $f_{BC} = 0.07$ [155]. In the backscattering direction, the results for the Mueller matrix element F_{22} correspond to a linear depolarisation ratio of about $\delta_l = 0.03$, which is rather low. In a follow-up study [156], δ_l has been modelled for two different volume fraction, $f_{BC} = 0.07$ and 0.20, three different wavelengths, $\lambda = 304$ nm, 533 nm, and 1010 nm, for different radii of the composite particle between 0.1 and 0.5 μm , and for different stochastic realisations of the aggregate geometry with prescribed fractal parameters. Unlike the optical cross sections, SSA, and g , the linear depolarisation ratio was found to vary among coated aggregates with different stochastic realisations of the geometry. Thus, when modelling δ_l , one always needs to average the optical properties over an ensemble of stochastic geometries. Further, the variation of δ_l among different realisations of the aggregate geometry needs to be quantified as part of the error estimate of the optics model. The model simulations in [155,156] were later compared to field measurements with NASA Langley airborne High Spectral Resolution Lidar [201]. The simulations were roughly consistent in the visible and NIR, but too low in the UV part of the spectrum.

In [158] a completely different model has been proposed in which the coating was assumed to form a film following the shape of the aggregate. For a volume fraction of $f_{BC} = 0.6$, $N_s = 100$, $D_f = 1.8$, $a = 20$ nm, and a wavelength $\lambda = 0.55$, the result reported for the F_{22} element of the Mueller matrix corresponds to a linear backscatter depolarisation ratio of about $\delta_l = 0.02$, which is very close to bare aggregates.

Depolarisation ratios modelled with a closed-cell model, a dimer of encapsulated aggregates, and a concentric core-shell spheroid were compared in [202]. The models yield results consistent with reported lidar field observations at 355, 532, and 1064 nm [201] only if the particle contains sufficient amount of weakly absorbing material, and if the overall shape deviates significantly from that of a sphere.

A wide selection of model particles were compared for two different aggregate sizes $N_s = 125$ and 422, two coating materials, volume fractions $f_{BC} = 7$ and 15 %, and at three wavelength (355, 532, and 1064 nm) [191]. Results for the linear depolarisation ratio varied widely among particle models. Several models yielded unrealistically low values of δ_l . Among the models that gave higher values of δ_l were a BC aggregate partially embedded in a sulphate or brown carbon host sphere, the closed cell model, and a dimer of BC aggregates embedded in spherical host particles.

In [190] a first attempt was made to construct a model that unifies the idea of film-coating and of encapsulated geometries. The particles were constructed such that coating is first applied as a thin film onto the aggregate. Then, as more and more coating is added, the shape of the coating gradually becomes more spherical. The computations were compared with published results from lidar field observations. For intermediate BC volume fractions and particle sizes, the model predicts δ_l values that are generally consistent with the observations. However, for low BC volume fractions (i.e., for heavily coated BC) and for larger particle sizes, the model predicts δ_l values that are higher than published measurements. The study concluded that it is, most likely, the non-sphericity of the coating that causes the overestimation of δ_l , since the model requires a very high amount of coating before the shell reaches perfect spherical shape. In [161] a coating model was proposed that mimicked the effect of surface tension of the coating. Similar to the model particles in [190], the coating shell reached spherical shape only for very high coating thicknesses, and the simulated values of δ_l had a tendency to overshoot the range of reported literature values. This supports the conclusion in [190], namely, that the shape of the coating is essential for modelling δ_l . This hypothesis was clearly formulated and tested in [70], which resulted in a coated aggregate model with a tunable transition from film-coating to encapsulated geometries. This model will be discussed in detail in Section 8.

6. Toward a physical understanding of the relation between aerosol morphology and aerosol optics

In many existing studies, morphologically sophisticated models for soot aggregates have been employed for quantifying the optical properties and the enhancement factor of the coating. This question is most important from a practical point of view, not least from a climate-modelling perspective. However, from a more fundamental point of view it is imperative to understand the physical processes that give rise to the optical properties. In particular, we want to gain physical insight into the relation between morphological and optical properties. Most importantly, we need to identify those morphological features that have the strongest impact on optical properties, and those that only cause minor changes.

It was noted in [18] and, more explicitly in [8,155] that the main morphological property that determines the absorption cross section of BC is the amount of material that interacts with the electromagnetic field. For a sufficiently large homogeneous sphere composed of highly absorbing material, such as BC, the electromagnetic field is quickly attenuated inside the sphere. (This effect may be somewhat weaker in the UV part of the spectrum, where the imaginary part of the refractive index of BC is lower.) As a result, much of the material near the centre of the sphere does not get in contact with the field and, consequently, does not contribute to absorption. By contrast, in a lacy fractal aggregate the BC material is distributed such that only little of the total aggregate mass is screened from interacting with the field. By this it has been explained why lacy aggregates have higher MAC values than compact ones, and why compact aggregates have higher MAC values than homogeneous spheres [8]. This explanation is corroborated by modelling calculations of the absorption inside aggregates and spheres [197]. Based on this physical understanding, the core grey shell model has been devised [155] as a simple and numerically efficient model for coated BC aggregates, which allows to smoothly tune the amount of BC material that interacts with the electromagnetic field, thus contributing to MAC. This model will be described in more detail in Section 7.

Understanding the interplay of morphology and polarisation of light poses a much greater challenge than understanding absorption properties. However, recent work [70,156,161,190,200,202] has

Table 1

Free tuning parameter in the CGS model as a function of wavelength, based on [156].

λ [μm]	0.232	0.304	0.393	0.533	0.702	> 1.000
f_{core}	0.7	0.7	0.6	0.5	0.5	0.1

allowed us to better understand which morphological properties have a dominant impact on the depolarisation properties of coated BC aggregates. As mentioned in the previous section, our present understanding is that the shape (spherical or nonspherical) of the coating is essential for the depolarisation ratio. It is well understood that even particles that only slightly deviate from spherical shape can cause significant depolarisation (e.g. [203,204]). Thus, the degree of nonsphericity of the coating constitutes a feature that can be exploited as a sensitive tuning parameter [70]. A model that makes use of this idea is discussed in Section 8.

7. Core grey shell (CGS) model for simulating optical cross sections of coated BC aggregates

The CGS model and its basic idea is illustrated in Fig. 2. It is based on the notion that a core-shell model (Fig. 2a) underestimates absorption, because much of the BC mass is shielded from interacting with the external field. By contrast, in a homogeneous “grey sphere” (Fig. 2d), in which BC and the coating material are homogeneously mixed, too much BC mass gets in contact with the field, resulting in too much absorption. In the CGS model, only a fraction f_{core} of the BC mass is put into the core, while the remaining BC mass fraction $(1 - f_{\text{core}})$ is homogeneously mixed with the coating. For $f_{\text{core}} = 1$, we retrieve the conventional core-shell model; for $f_{\text{core}} = 0$ we obtain the homogeneous grey-sphere model. Thus, these two models are included in the CGS model as limiting cases. By varying f_{core} from 1 to 0 we can continuously tune the model and obtain a gradual transition from the core-shell to the homogeneous grey-sphere model (Fig. 2, a–d). In this transition, the core becomes steadily smaller, while the shell becomes more and more grey. As a result, an increasingly larger fraction of the BC mass gets in contact with the external field, resulting in increased absorption.

The CGS model has been tested by comparison to a realistic model of sulphate-coated fractal aggregates [156]. The computations were performed for the spectral range from 230 nm to 8.0 μm, for composite volume-equivalent particle radii in the range $r_v = 0.1$ –0.5 μm, and for BC volume fraction $f_{\text{BC}} = 0.07$ and 0.20. The CGS model outperformed both the core-shell and the homogeneous grey-sphere model (where the effective refractive index had been computed by Maxwell-Garnett EMT). It was shown that the free parameter f_{core} could be tuned for each wavelength such that the model closely fitted the reference results obtained with the coated-aggregate model. The best choice of f_{core} for each wavelength reported in [156] is reproduced in Table 1. Remarkably enough, the CGS model turned out to not only fit C_{abs} , but also SSA, g , and C_{bak} with high accuracy. The choice of f_{core} only depended on λ ; it was independent of particle size, BC volume fraction f_{BC} , and of the optical parameter being fitted.

The CGS model is based on the plausible hypothesis that interpolation between the two extreme cases, the core-shell and the homogeneous grey-sphere model, should yield a tunable model for fitting optical parameters. We demonstrate this here in Fig. 3, which shows computational results for C_{abs} (top row), SSA (second row), g (third row), and C_{bak} (bottom row) as a function of volume-equivalent radius r_v obtained for BC volume fractions of $f_{\text{BC}} = 0.07$ (left column) and 0.20 (right column). The wavelength of light is $\lambda = 533$ nm. The reference computations (black lines) are based on a coated fractal aggregate model as described in [156]. The red line

shows corresponding results obtained with the CGS model with $f_{\text{core}} = 0.5$ (see Table 1). The pink shading shows the range of results obtained by varying f_{core} between 0 and 1. Results obtained with the homogeneous grey-sphere and the core-shell model are indicated by the dashed and solid blue lines, respectively. It is evident that the homogeneous grey-sphere and the CGS models yield, indeed, extreme values of C_{abs} , SSA, and g , between which the CGS model interpolates. In most cases, the coated aggregate model falls within the range covered by the CGS model. Indeed, the CGS model with $f_{\text{core}} = 0.5$ lies very close to the reference results. The only exception is SSA in the size range 200–350 nm, in which all models underestimate the reference results. The backscatter cross section C_{bak} displays a rather remarkable behaviour, particularly for $f_{\text{BC}} = 0.07$ (bottom left). Both the core-shell and, even more so, the homogeneous grey-sphere model overestimate C_{bak} . Nevertheless, the reference results lie within the range of CGS results; the CGS computations for $f_{\text{core}} = 0.5$ follow the reference results closely. Thus the CGS model, although designed to fit C_{abs} , also performs well for modelling SSA, g , and even the differential scattering property C_{bak} .

Fig. 4 shows results analogous to those in Fig. 3, but as a function of wavelength λ for a fixed particle radius $r_v = 500$ nm. In general, the core-shell model does not provide a good fit of the optical properties of the coated-aggregates. The asymmetry parameter g is least sensitive to the choice of particle model, while the backscatter cross section is strongly sensitive over the full spectral range. C_{abs} and SSA are most sensitive in the spectral range from 0.2 to 1.0 μm . The homogeneous grey-sphere model only gives a reasonable representation of C_{abs} for a BC volume fraction $f_{\text{BC}} = 0.20$, but it overestimates C_{abs} for $f_{\text{BC}} = 0.07$. By contrast, the CGS model, properly tuned according to Table 1, faithfully represents all four optical parameters for both BC volume fractions over the entire spectral range.

These results illustrate the potential of the CGS model. It has all the required features of a versatile simple model particle, i.e., this model

- simplifies the morphology as far as possible;
- has a small number of free tuning parameters (namely, a single parameter f_{core});
- covers a large range of values by varying the tuning parameter; and
- is capable of reproducing several optical parameters for a range of particle sizes, wavelengths, and compositions.

The high degree of symmetry of these particles is essential for computational speed in light scattering computations (e.g. [107,108]).

The model has, so far, been integrated into the aerosol optics module of the chemical transport model MATCH (Multiple-scale Atmospheric Transport and CHemistry modelling system) [19]. It has been applied to investigation of the information content of lidar observations [205,206] and to assimilation of CALIOP extinction profiles into MATCH [207].

8. Tunable model for simulating depolarisation by coated BC aggregates

The main principle of this model is illustrated in Fig. 5. We start from a bare BC aggregate, and we imagine a sphere with diameter D_c that partially contains the aggregate. For instance, we can take the maximum diameter D of the aggregate and scale it with a factor f_c , so that our imaginary sphere has diameter $D_c = f_c D$. Next, we add a thin film of coating material with a pre-defined coating thickness d_c closely following the shape of the aggregate. If using the DDA, the coating thickness can be set equal to the dipole spacing, $d_c = d$. The coating is constrained to lie inside the sphere of

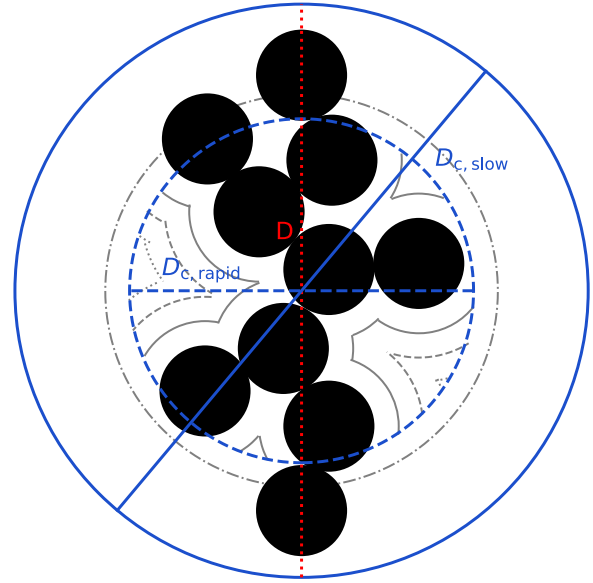


Fig. 5. Coated soot model with tunable transition speed.

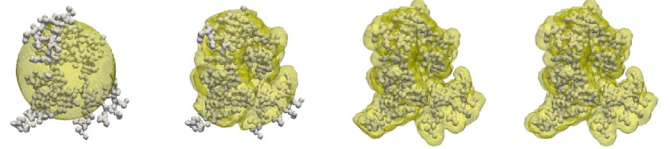


Fig. 6. Coated aggregates ($N_s = 512$, $D_f = 2.4$, $k_0 = 0.7$, cluster-cluster algorithm) with $f_{\text{vol}} = 0.1$. Parameter f_c changed: 0.5, 0.75, 1.0, 1.25 (left to right)

diameter D_c . If all monomers inside the sphere are coated, then we add another coating layer of thickness d_c , again constrained to lie inside the imaginary sphere. The procedure is continued until a prescribed BC volume fraction f_{BC} is reached. If the sphere of Diameter D_c is completely filled before f_{BC} is reached, then subsequent coating layers of thickness f_c are added onto the sphere. The coating makes a gradual transition from film-coating to a radially growing sphere. The smaller $D_c = f_c D$, the more “rapidly” this transition takes place, i.e., the less coating material is required to make the coating spherical. The free tuning parameter f_c can be used to control the shape of the coating. If f_c is small, then the coating becomes spherical very quickly as more coating material is added. If f_c is large, then the coating will be non-spherical even for thickly coated aggregates.

This is illustrated in Fig. 6. As f_c is increased from 0.5 to 0.75 and 1.0, the coating becomes strongly non-spherical. A further increase from $f_c = 1.0$ to 1.25 has no effect in this case ($f_{\text{BC}} = 0.1$), but it would have for lower values of f_{BC} .

The main idea behind this model is to tune the depolarisation properties. Aggregates with a perfect spherical coating have been hypothesised to depolarise only weakly [190] (since spheres do not depolarise, and BC aggregates depolarise only weakly). Aggregates with even mildly nonspherical coating are hypothesised to cause stronger depolarisation. This has been tested and confirmed in [70]. Fig. 7 illustrates this for the model particles shown in Fig. 6. For this particular BC volume fraction $f_{\text{BC}} = 0.1$, the coating is spherical for $f_c \leq 0.6$. Indeed, δ_l is low and independent of f_c for $f_c \leq 0.6$. As soon as f_c is made large enough so that the coating becomes even mildly nonspherical, δ_l increases steeply with f_c . It reaches a maximum around $f_c = 0.8$, and beyond $f_c = 1.0$ it does not change anymore. This is because for $f_{\text{BC}} = 0.1$, the circumscribed

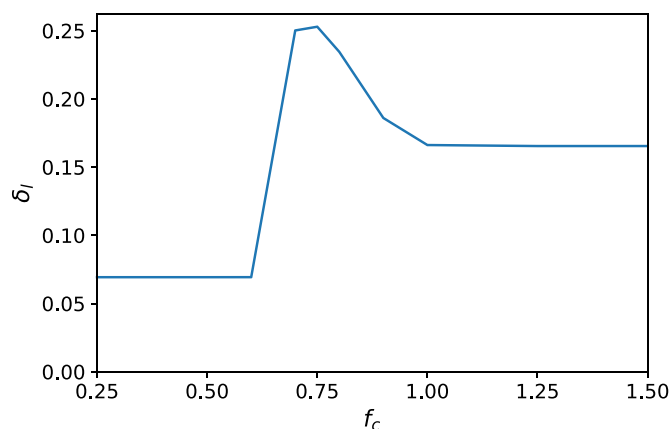


Fig. 7. Depolarisation as function of f_c , four of the geometries used, are shown in Fig. 6.

ing sphere has no constraining effect on the shape of the coating for $f_c > 1.0$.

In this example, by varying f_c between 0.6 and 1.0 one covers a range of δ_l between 0.07 and 0.25. Thus, this model is capable of covering a large range of δ_l values by varying a single tuning parameter. However, it is computationally expensive, since the particles lack symmetry. A first application of the model has been reported recently [200], in which the sensitivity of δ_l and other optical properties to the composition of the coating material has been studied.

9. Summary and recommendations

Modelling the optical properties of bare black carbon aggregates has reached a high degree of maturity. The impact on optical properties of number and size of monomers, dielectric properties, fractal parameters, monomer polydispersity and nonsphericity, as well as overlapping and necking have been extensively studied. As demonstrated in [64], the impact of minor geometric structures on optical properties derives, to a large extent, from their impact on the particle volume.

- The volume effect of minor structures on the optical properties should be accounted for as explained in [64]. When doing so, the optical cross sections of bare fractal aggregates can be quite accurately modelled by use of a fractal aggregate model of monodisperse monomers in point contact. The remaining error (not explained by the volume effect) introduced by neglecting minor structures is on the order of 5 %; it can be accounted for by a simple bias correction [64].

Optical properties of black carbon aggregates mixed with other material, such as sulphate, organic carbon, sea salt, or water, are challenging to model accurately. The absorption cross section and, related to that, the absorption enhancement factor, depend on the amount of BC mass that interacts with the incident field. In a compact core-shell model, an unrealistically high amount of the BC mass is shielded from the external field by the obstructing effect of BC near the surface of the sphere. However, it has been demonstrated that the core grey shell (CGS) model provides us, by introducing a single free parameter, with a class of spherically symmetric core-mantel model geometries that encompass a large range of absorption and scattering cross sections, single scattering albedos, asymmetry parameters, and backscattering cross sections. Thus, our recommendation is:

- The conventional core-shell model should be retired as a reference geometry. It should be replaced by the CGS model as a

reference model in future studies on optical properties of encapsulated BC aerosols.

(This situation is similar to mineral dust aerosols, where homogeneous spheres are clearly unfit for mimicking optical properties. However, by introducing a single free parameter (the aspect ratio), one has replaced spheres by spheroids, which have been demonstrated to provide a significantly improved representation of dust optical properties compared to spheres [208,209]).

Our understanding of the relation between morphological properties and the linear depolarisation ratio δ_l of encapsulated BC aerosols has significantly improved. According to our present state of knowledge, the shape of the mantel has a dominant impact on δ_l . Model particles in which the mantel retains a non-spherical shape even for heavily coated BC aggregates tend to overestimate δ_l [161,190]. A recently introduced tunable model [70] is tailored to cover a large range of δ_l values by varying a single parameter that impacts the shape of the coating.

- Future studies on the depolarisation properties of coated BC aggregates should aim at further investigating the hypothesis that δ_l is predominantly determined by the shape of the mantel.

The long-term goal should be to develop a model for computing depolarisation by coated BC aerosols suitable for large-scale applications.

Declaration of Competing Interest

The authors declare that they have no known competing financial interests or personal relationships that could have appeared to influence the work reported in this paper

Acknowledgements

We acknowledge funding by the Swedish National Space Agency (Rymdstyrelsen) under contract 100/16 (MK) and by the Swedish Research Council (Vetenskapsrådet) under contract 2016-03499 (FK). The calculations were partly performed on resources at Chalmers Centre for Computational Science and Engineering (C3SE) provided by the Swedish National Infrastructure for Computing (SNIC). We are grateful to Dan Mackowski and Michael Mishchenko for making their MSTM code publicly available, and to Dan Mackowski for providing his cluster-cluster aggregation algorithm. Alfons G. Hoekstra and Maxim A. Yurkin are acknowledged for making their ADDA code publicly available.

References

- [1] Ramanathan V, Carmichael G. Global and regional climate changes due to black carbon. *Nat Geosci* 2008;1:221–7.
- [2] Myhre G, Shindell D, Breon F-M, Collins W, Fuglestad J, Huang J, et al. Anthropogenic and natural radiative forcing. In: Stocker T, Qin D, Plattner G-K, Tignor M, Allen S, Boschung J, et al., editors. *Climate change 2013: the physical science basis. contribution of working group I to the fifth assessment report of the intergovernmental panel on climate change*. Cambridge, United Kingdom and New York, NY, USA: Cambridge University Press; 2013. p. 659–740. doi:10.1017/CBO9781107415324.018. ISBN 978-1-107-66182-0
- [3] Bond TC, Doherty SJ, Fahey DW, Forster PM, Bernsten T, DeAngelo BJ, et al. Bounding the role of black carbon in the climate system: a scientific assessment. *J Geophys Res* 2013;118:5380–552.
- [4] Pöschl U. Atmospheric aerosols: Composition, transformation, climate and health effects. *Angew Chem Int Ed* 2005;44:7520–40.
- [5] Anenberg SC, Talgo K, Arunachalam S, Dolwick P, Jang C, West JJ. Impacts of global, regional, and sectoral black carbon emission reductions on surface air quality and human mortality. *Atmos Chem Phys* 2011;11:7253–67.
- [6] Anenberg SC, Schwartz J, Shindell D, Amann M, Faluvegi G, Janssens-Maenhout ZKG, et al. Global air quality and health co-benefits of mitigating near-term climate change through methane and black carbon emission controls. *Environ Health Perspect* 2012;120:831–9.
- [7] Kahnert M. Numerically exact computation of the optical properties of light absorbing carbon aggregates for wavelength of 200 nm 12.2 μm. *Atmos Chem Phys* 2010;10:8319–29.

- [8] Kahnert M, Devasthale A. Black carbon fractal morphology and short-wave radiative impact: a modelling study. *Atmos Chem Phys* 2011;11:11745–59.
- [9] Zeng C, Liu C, Li J, Zhu B, Yin Y, Wang Y. Optical properties and radiative forcing of aged bc due to hygroscopic growth: Effects of the aggregate structure. *J Geophys Res* 2019;124(8):4620–33. doi:10.1029/2018JD029809.
- [10] Jacobson MZ. A physically-based treatment of elemental carbon optics: Implications for global direct forcing of aerosols. *Geophys Res Lett* 2000;27:217–20.
- [11] Jacobson MZ. Global direct radiative forcing due to multicomponent anthropogenic and natural aerosols. *J Geophys Res* 2001;106:1551–68.
- [12] Jacobson MZ. Strong radiative heating due to the mixing state of black carbon in atmospheric aerosols. *Nature* 2001;409:695–7.
- [13] Schnaiter M, Linke C, Moehler O, Naumann K-H, Saathoff H, Wagner R, et al. Absorption amplification of black carbon internally mixed with secondary organic aerosol. *J Geophys Res* 2005;110. doi:10.1029/2005JD006046. D19204.
- [14] Khalizov AF, Xue H, Wang L, Zheng J, Zhang R. Enhanced light absorption and scattering by carbon soot aerosol internally mixed with sulfuric acid. *J Phys Chem A* 2009;113:1066–74.
- [15] Cappa CD, Onasch TB, Massoli P, Worsnop DR, Bates TS, Cross ES, et al. Radiative absorption enhancements due to the mixing state of atmospheric black carbon. *Science* 2012;337:1078–81.
- [16] Zhang X, Mao M, Yin Y, Wang B. Numerical investigation on absorption enhancement of black carbon aerosols partially coated with nonabsorbing organics. *J Geophys Res* 2018;123(2):1297–308. doi:10.1002/2017JD027833.
- [17] Benedetti A, Morcrette MJ-J, Boucher O, Dethof A, Engelen RJ, Huneeus MFHFN, et al. Aerosol analysis and forecast in the European centre for medium-range weather forecasts integrated forecast system: 2. data assimilation. *J Geophys Res* 2009;114:D13205.
- [18] Kahnert M. Modelling the optical and radiative properties of freshly emitted light absorbing carbon within an atmospheric chemical transport model. *Atmos Chem Phys* 2010;10:1403–16.
- [19] Andersson E, Kahnert M. Coupling aerosol optics to the MATCH (v5. 5.0) chemical transport model and the SALSA (v1) aerosol microphysics module. *Geosci Model Dev* 2016;9:1803–26.
- [20] Rodgers CD. Inverse methods for atmospheric sounding. Singapore: World Scientific; 2000.
- [21] Ansmann A, Müller D. Lidar and atmospheric aerosol particles. In: Weitkamp C, editor. *Lidar. Springer Series in Optical Sciences*, 102. New York, NY: Springer; 2005. p. 105–41.
- [22] David G, Thomas B, Nousiainen T, Miffre A, Rairoux P. Retrieving simulated volcanic, desert dust and sea-salt particle properties from two/three-component particle mixtures using UV-VIS polarization lidar and T matrix. *Atmos Chem Phys* 2013;13:6757–76. doi:10.5194/acp-13-6757-2013.
- [23] Burton SP, Vaughan MA, Ferrare RA, Hostetler CA. Separating mixtures of aerosol types in airborne High Spectral Resolution Lidar data. *Atmos Meas Tech* 2014;7:419–36.
- [24] Burton SP, Chemyakin E, Liu X, Knobelspiesse K, Stamnes S, Sawamura P, et al. Information content and sensitivity of the $3\beta + 2\alpha$ lidar measurement system for aerosol microphysical retrievals. *Atmos Meas Techniques* 2016;9:5555–74.
- [25] Sorensen CM. Light scattering by fractal aggregates: a review. *Aerosol Sci Technol* 2001;35:648–87.
- [26] Liu C. Optical properties of black carbon aggregates. In: Kokhanovsky A, editor. *Springer series in light scattering: volume 3: radiative transfer and light scattering*. Cham: Springer International Publishing; 2019. p. 167–218.
- [27] He C. Radiative properties of atmospheric black carbon (soot) particles with complex structures. In: Kokhanovsky A, editor. *Springer series in light scattering: volume 4: light scattering and radiative transfer*. Cham: Springer International Publishing; 2019. p. 219–54.
- [28] Mishchenko MI, Travis LD, Lacis AA. Scattering, absorption, and emission of light by small particles. Cambridge: Cambridge University Press; 2002.
- [29] Kahnert M. Numerical solutions of the macroscopic Maxwell equations for scattering by non-spherical particles: A tutorial review. *J Quant Spectrosc Radiat Transfer* 2016;178:22–37.
- [30] Forrest SR, Witten TA. Long-range correlations in smoke-particle aggregates. *J Phys A* 1979;12:L109–17.
- [31] Sorensen CM, Roberts GM. The prefactor of fractal aggregates. *J Colloid Interface Sci* 1997;186:447–52.
- [32] Jones AR. Light scattering in combustion. In: Kokhanovsky A, editor. *Light Scattering Reviews*; 2006. p. 393–444.
- [33] Eggersdorfer ML, Pratsinis SE. The structure of agglomerates consisting of polydisperse particles. *Aerosol Sci Technol* 2012;46:347–53.
- [34] Schnaiter M, Horvath H, Möhler O, Naumann K-H, Saathoff H, Schöck OW. UV-VIS-NIR spectral optical properties of soot and soot-containing aerosols. *J Aerosol Sci* 2003;34:1421–44.
- [35] He C, Liou K-N, Takano Y, Zhang R, Levy Zamora M, Yang P, et al. Variation of the radiative properties during black carbon aging: theoretical and experimental intercomparison. *Atmos Chem Phys* 2015;15:11967–80.
- [36] Hallett J, Hudson JG, Rogers CF. Characterization of combustion aerosols for haze and cloud formation. *Aerosol Sci Technol* 1989;10:70–83.
- [37] Colbeck I, Appleby L, Hardman EJ, Harrison RM. The optical properties and morphology of cloud-processed carbonaceous smoke. *J Aerosol Sci* 1990;21:527–38.
- [38] Ramachandran G, Reist PC. Characterization of morphological changes in agglomerates subject to condensation and evaporation using multiple fractal dimensions. *Aerosol Sci Technol* 1995;23:431–42.
- [39] Nyeki S, Colbeck I. Fractal dimension analysis of single, in-situ, restructured carbonaceous aggregates. *Aerosol Sci Technol* 1995;23:109–20.
- [40] Pei X, Hallquist M, Eriksson AC, Pagels J, Donahue NM, Mentel T, et al. Morphological transformation of soot: investigation of microphysical processes during the condensation of sulfuric acid and limonene ozonolysis product vapors. *Atmos Chem Phys* 2018;18:9845–60.
- [41] Bambha RP, Dansson MA, Schrader PE, Michelsen HA. Effects of volatile coatings and coating removal mechanisms on the morphology of graphitic soot. *Carbon* 2013;61:80–96. doi:10.1016/j.carbon.2013.04.070.
- [42] Ghazi R, Olfert JS. Coating mass dependence of soot aggregate restructuring due to coatings of oleic acid and dioctyl sebacate. *Aerosol Sci Technol* 2013;47(2):192–200. doi:10.1080/02786826.2012.741273.
- [43] Schnitzler EG, Dutt A, Charbonneau AM, Olfert JS, Jger W. Soot aggregate restructuring due to coatings of secondary organic aerosol derived from aromatic precursors. *Environ Sci Technol* 2014;48(24):14309–16. doi:10.1021/es503699b. PMID: 25390075.
- [44] Zhang R, Khalizov AF, Pagels J, Zhang D, Xue H, McMurphy PH. Variability in morphology, hygroscopicity, and optical properties of soot aerosols during atmospheric processing. *Proc Natl Acad Sci USA* 2008;105(30):10291–6. doi:10.1073/pnas.0804860105.
- [45] Schnitzler EG, Gac JM, Jger W. Coating surface tension dependence of soot aggregate restructuring. *J Aerosol Sci* 2017;106:43–55. doi:10.1016/j.jaerosci.2017.01.005.
- [46] Wentzel M, Gorzawski G, Naumann K-H, Saathoff H, Weinbruch S. Transmission electron microscopical and aerosol dynamical characterization of soot aerosols. *Aerosol Sci* 2003;34:1347–70.
- [47] Skillas G, Knel S, Burtscher H, Baltensperger U, Siegmann K. High fractal-like dimension of diesel soot agglomerates. *J Aerosol Sci* 1998;29(4):411–19. doi:10.1016/S0021-8502(97)00448-5.
- [48] Mikhailov EF, Vlasenko SS, Podgorny IA, Ramanathan V, Corrigan CE. Optical properties of soot-water drop agglomerates: An experimental study. *J Geophys Res* 2006;111. doi:10.1029/2005JD006389. D07209.
- [49] van Poppel LH, Friedrich H, Spinsby J, Chung SH, Seinfeld JH, Buseck PR. Electron tomography of nanoparticle clusters: Implications for atmospheric lifetimes and radiative forcing of soot. *Geophys Res Lett* 2005;32. doi:10.1029/2005GL024461. L24811.
- [50] Adachi K, Chung SH, Friedrich H, Buseck PR. Fractal parameters of individual soot particles determined using electron tomography: Implications for optical properties. *J Geophys Res* 2007;112. doi:10.1029/2006JD008296. D14202.
- [51] Köylü ÜÖ, Faeth GM. Structure of overfire soot in buoyant turbulent diffusion flames at long residence times. *Combust Flame* 1992;89:140–56.
- [52] Lee KO, Cole R, Sekar R, Choi MY, Kang JS, Bae CS, et al. Morphological investigation of the microstructure, dimensions, and fractal geometry of diesel particulates. *Proc Combust Inst* 2002;29:647–53.
- [53] Adachi K, Chung S, Buseck PR. Shapes of soot aerosol particles and implications for their effects on climate. *J Geophys Res* 2010;115. doi:10.1029/2009JD012868. D15206.
- [54] Farias TL, Köylü ÜÖ, Carvalho MG. Effects of polydispersity of aggregates and primary particles on radiative properties of simulated soot. *J Quant Spectrosc Radiat Transfer* 1996;55:357–71.
- [55] Liu C, Yin Y, Hu F, Jin H, Sorensen CM. The effect of monomer size distribution on the radiative properties of black carbon aggregates. *Aerosol Sci Technol* 2015;49:928–40.
- [56] Yon J, Liu F, Morán J, Fuentes A. Impact of the primary particle polydispersity on the radiative properties of soot aggregates. *Proc Combust Inst* 2019;37:1151–9.
- [57] Li J, Anderson JR, Buseck PR. TEM study of aerosol particles from clean and polluted marine boundary layers over the North Atlantic. *J Geophys Res* 2003;108. doi:10.1029/2002JD002106. ACH 8–1 – 8–11.
- [58] Dobbins R, Megaridis C. Morphology of flame-generated soot as determined by thermophoretic sampling. *Langmuir* 1987;3:254–9.
- [59] Megaridis CM, Dobbins RA. Morphological description of flame-generated materials. *Combust Sci Technol* 1990;71:95–109.
- [60] Yon J, Bescond A, Liu F. On the radiative properties of soot aggregates part 1: Necking and overlapping. *J Quant Spectrosc Radiat Transfer* 2015;162:197–206.
- [61] Skorupski K, Mroczka J, Riefler N, Oltmann H, Will S, Wriedt T. Impact of morphological parameters onto simulated light scattering patterns. *J Quant Spectrosc Radiat Transfer* 2013;119:53–66.
- [62] Liu F, Yon J, Bescond A. On the radiative properties of soot aggregates — part 2: effects of coating. *J Quant Spectrosc Radiat Transfer* 2016;172:134–45.
- [63] Doner N, Liu F. Impact of morphology on the radiative properties of fractal soot aggregates. *J Quant Spectrosc Radiat Transfer* 2017;187:10–19.
- [64] Teng S, Liu C, Schnaiter M, Chakrabarty RK, Liu F. Accounting for the effects of nonideal minor structures on the optical properties of black carbon aerosols. *Atmos Chem Phys* 2019;19:2917–31.
- [65] Bescond A, Yon J, Girasole T, Jouen C, Rozé C, Coppalle A. Numerical investigation of the possibility to determine the primary particle size of fractal aggregates by measuring light depolarization. *J Quant Spectrosc Radiat Transfer* 2013;126:130–9.
- [66] Skorupski K, Mroczka J. Effect of the necking phenomenon on the optical properties of soot particles. *J Quant Spectrosc Radiat Transfer* 2014;141:40–8.
- [67] Brasil A, Farias T, Carvalho M. A recipe for image characterization of fractal-like aggregates. *J Aerosol Sci* 1999;30:1379–89.
- [68] Oh C, Sorensen CM. The effect of overlap between monomers on the determination of fractal cluster morphology. *J Colloid Interface Sci* 1997;193:17–25.

- [69] China S, Mazzoleni C, Gorkowski K, Aiken AC, Dubey MK. Morphology and mixing state of individual freshly emitted wildfire carbonaceous particles. *Nat Commun* 2013;4:2122. doi:10.1038/ncomms3122.
- [70] Kannigieser F, Kahnert M. Calculation of optical properties of light-absorbing carbon with weakly absorbing coating: A model with tunable transition from film-coating to spherical-shell coating. *J Quant Spectrosc Radiat Transfer* 2018;2016:17–36.
- [71] Adler G, Riziq AA, Erlick C, Rudich Y. Effect of intrinsic organic carbon on the optical properties of fresh diesel soot. *PNAS* 2009;107:6699–704.
- [72] Chen Y, Bond TC. Light absorption by organic carbon from wood combustion. *Atmos Chem Phys* 2010;10:1773–87.
- [73] Chen D, Liu Z, Schwartz CS, Lin H-C, Cetola JD, Gu Y, et al. The impact of aerosol optical depth assimilation on aerosol forecasts and radiative effects during a wild fire event over the United States. *Geosci Model Dev* 2014;7:2709–15.
- [74] Chakrabarty RK, Beres ND, Moosmüller H, China S, Mazzoleni C, Dubey MK, et al. Soot superaggregates from flaming wildfires and their direct radiative forcing. *Sci Rep* 2014;4:5508. doi:10.1038/srep05508.
- [75] Wilson J, Cuvelier C, Raes F. A modeling study of global mixed aerosol fields. *J Geophys Res* 2001;106:34081–108.
- [76] Naoe H, Okada K. Mixing properties of submicrometer aerosol particles in the urban atmosphere – with regard to soot particles. *Atmos Env* 2001;35:5765–72.
- [77] Adachi K, Buseck PR. Internally mixed soot, sulfates, and organic matter in aerosol particles from Mexico City. *Atmos Chem Phys* 2008;8:6469–81.
- [78] Shiraiwa M, Kondo Y, Iwamoto T, Kita K. Amplification of light absorption of black carbon by organic coating. *Aerosol Sci Technol* 2010;44:46–54.
- [79] Smekens A, Pauwels J, Berghmans P, Grieken RV. Correlation study between the aerodynamic diameter and the number of primary particles of soot aggregates by STEM. *J Aerosol Sci* 1997;28:761–2.
- [80] Liu C, Panetta RL, Yang P, Macke A, Baran AJ. Modeling the scattering properties of mineral aerosols using concave fractal polyhedra. *Appl Opt* 2012;52:640–52.
- [81] Mishchenko MI, Liu L, Cairns B, Mackowski DW. Optics of water cloud droplets mixed with black-carbon aerosols. *Opt Lett* 2014;39:2607–10.
- [82] Cheng T, Gu X, Wu Y, Chen H. Effects of atmospheric water on the optical properties of soot aerosols with different mixing states. *J Quant Spectrosc Radiat Transfer* 2014;147:196–206.
- [83] Riemer N, Vogel H, Vogel B. Soot aging time scales in polluted regions during day and night. *Atmos Chem Phys* 2004;4:1885–93.
- [84] Tsyro S, Simpson D, Tarrasón L, Kupiainen ZKK, Pio C, Yttri KE. Modelling of elemental carbon over Europe. *J Geophys Res* 2007;112. D23S19.
- [85] Liu L, Mishchenko MI. Scattering and radiative properties of complex soot and soot-containing aggregate particles. *J Quant Spectrosc Radiat Transfer* 2007;106:262–73.
- [86] Wu Y, Cheng T, Zheng L, Chen H. Optical properties of the semi-external mixture composed of sulfate particle and different quantities of soot aggregates. *J Quant Spectrosc Radiat Transfer* 2016;179:139–48.
- [87] Sakamoto KM, Allan JD, Coe H, Taylor JW, Duck TJ, Pierce JR. Aged boreal biomass-burning aerosol size distributions from BORTAS 2011. *Atmos Chem Phys* 2015;15:1633–46.
- [88] Färnlund J, Holman K, Kägeson P. Emissions of ultrafine particles from different types of light duty vehicles. Tech. Rep., Borlänge: Swedish National Road Administration; 2001.
- [89] Tamm H, Mirme A, Tamm E. Electrical aerosol spectrometer of tartu university. *Atmos Res* 2015;62:315–24.
- [90] Strapp JW, Leaith WR, Liu PSK. Hydrated and dried aerosol-size-distribution measurements from the particle measuring system FSP-300 probe and the deiced PCASP-100X probe. *J Atmos Ocean Technol* 1992;9:548–55.
- [91] Vester BP, Ebert M, Barnert EB, Schneider J, Kandler K, Schütz L, et al. Composition and mixing state of the urban background aerosol in the Rhein-Main area (Germany). *Atmos Env* 2007;41:6102–15.
- [92] Pratt KA, Prather KA. Mass spectrometry of atmospheric aerosols: recent developments and applications. part ii: Online mass spectrometry techniques. *Mass Spectrom Rev* 2012;31:17–48.
- [93] Laborde M, Schnaiter M, Linke C, Saathoff H, Naumann K-H, Mohler O, et al. Single particle soot photometer intercomparison at the AIDA chamber. *Atmos Meas Tech* 2012;5:3077–97.
- [94] Bond TC, Bergstrom RW. Light absorption by carbonaceous particles: an investigative review. *Aerosol Sci Technol* 2006;40:27–67.
- [95] Robertson J. Hard amorphous (diamond-like) carbons. *Prog Solid St Chem* 1991;21:199–333.
- [96] Bond TC. Spectral dependence of visible light absorption by carbonaceous particles emitted from coal combustion. *Geophys Res Lett* 2001;28:4075–8.
- [97] Chang H, Charalampopoulos TT. Determination of the wavelength dependence of refractive indices of flame soot. *Proc R Soc Lond A* 1990;430:577–91.
- [98] Ahrenkiel RK. Modified Kramers-Kronig analysis of optical spectra. *J Opt Soc Am* 1971;61:1651–5.
- [99] Takano Y, Liou KN, Kahnert M, Yang P. The single-scattering properties of black carbon aggregates determined from the geometric-optics surface-wave approach and the t-matrix method. *J Quant Spectrosc Radiat Transfer* 2013;125:51–6.
- [100] Cheng T, Wu Y, Chen H. Effects of morphology on the radiative properties of internally mixed light absorbing carbon aerosols with different aging status. *Opt Express* 2014;22:15904–17.
- [101] Dong J, Zhao JM, Liu LH. Morphological effects on the radiative properties of soot aerosols in different internally mixing states with sulfate. *J Quant Spectrosc Radiat Transfer* 2015;165:43–55.
- [102] Ceolato R, Gaudfrin F, Pujol O, Riviere N, Berg MJ, Sorensen CM. Lidar cross-sections of soot fractal aggregates: Assessment of equivalent-sphere models. *J Quant Spectrosc Radiat Transfer* 2018;212:39–44.
- [103] Liu C, Chung CE, Yin Y, Schnaiter M. The absorption ångström exponent of black carbon: from numerical aspects. *Atmos Chem Phys* 2018;18:6259–73.
- [104] Krekov GM. Models of atmospheric aerosol. In: Jennings SG, editor. *Aerosol effects on climate*. Tucson, AZ: University of Arizona; 1993. p. 9–72.
- [105] d'Almeida GA, Koepke P, Shettle EP. *Atmospheric Aerosols*. Hampton, VA: DEEPACK; 1991.
- [106] Kirchstetter TW, Novakov T, Hobbs PV. Evidence that the spectral dependence of light absorption by aerosols is affected by organic carbon. *J Geophys Res* 2004;109:D21208.
- [107] Schulz FM, Stamnes K, Stamnes JJ. Point group symmetries in electromagnetic scattering. *J Opt Soc Am A* 1999;16:853–65.
- [108] Kahnert M. Irreducible representations of finite groups in the T matrix formulation of the electromagnetic scattering problem. *J Opt Soc Am A* 2005;22:1187–99.
- [109] Bohren CF, Huffman DR. *Absorption and scattering of light by small particles*. Weinheim: Wiley-VCH; 1983.
- [110] Dobbins RA, Megaridis CM. Absorption and scattering of light by polydisperse aggregates. *Appl Opt* 1991;30(33):4747–54.
- [111] Gangopadhyay S, Elminyawi I, Sorensen CM. Optical structure factor measurements of soot particles in a premixed flame. *Appl Opt* 1991;30(33):4859–64.
- [112] Krishnan SS, Lin K-C, Faeth GM. Optical properties in the visible of over-fire soot in large buoyant turbulent diffusion flames. *J Heat Transfer* 2000;122:517–24.
- [113] Sorensen CM, Yon J, Liu F, Maughan J, Heinson WR, Berg MJ. Light scattering and absorption by fractal aggregates including soot. *J Quant Spectrosc Radiat Transfer* 2018;217:459–73.
- [114] Naumann K-H. COSIMA—a computer program simulating the dynamics of fractal aerosols. *Aerosol Sci* 2003;34:1371–97.
- [115] Zhang J, Qi H. Retrieval of fractal dimension and size distribution of non-compact soot aggregates from relative intensities of multi-wavelength angular-resolved light scattering. *Opt Express* 2019;27:1613–31.
- [116] Farias TL, Köylü ÜÖ, Carvalh MG. Range of validity of the rayleighdebye-gans theory for optics of fractal aggregates. *Appl Opt* 1996;33:6560–7.
- [117] Zhao Y, Ma L. Assessment of two fractal scattering models for the prediction of the optical characteristics of soot aggregates. *J Quant Spectrosc Radiat Transfer* 2009;110:315–22.
- [118] Soewono A, Rogak SN. Morphology and optical properties of numerically simulated soot aggregates. *Aerosol Sci Technol* 2013;47:267–74.
- [119] Wang G, Sorensen CM. Experimental test of the Rayleigh-Debye-Gans theory for light scattering by fractal aggregates. *Appl Opt* 2002;22:4645–51.
- [120] Chakrabarty RK, Moosmüller H, Arnott WP, Garro MA, Slowik JG, Cross ES, et al. Light scattering and absorption by fractal-like carbonaceous chain aggregates: comparison of theories and experiment. *Appl Opt* 2007;46:6990–7006.
- [121] Iskander MF, Chen HY, Penner JE. Resonance optical absorption by fractal agglomerates of smoke aerosols. *Atmos Environ* 1991;25:2563–9.
- [122] Lakhtakia A, Mulholland GW. On two numerical techniques for light scattering by dielectric agglomerated structures. *J Res Natl Inst Stand Technol* 1993;98:699–716.
- [123] Mulholland GW, Bohren CF, Fuller KA. Light scattering by agglomerates: coupled electric and magnetic dipole method. *Langmuir* 1994;10:2533–46.
- [124] Yon J, Rozé C, Girasole T, Coppalle A, Mées L. Extension of RDG-FA for scattering prediction of aggregates of soot taking into account interactions of large monomers. *Part Part Syst Charact* 2008;25:54–67.
- [125] Yon J, Liu F, Bescond A, Caumont-Prim C, Rozé C, Ouf FX, et al. Effects of multiple scattering on radiative properties of soot fractal aggregates. *J Quant Spectrosc Radiat Transfer* 2014;133:374–81.
- [126] Karlsson A, Bladh H, Bengtsson P-E. Accurate method for predicting light scattering from soot aggregates with subparticles of arbitrary shape and structure. *J Opt Soc Am A* 2009;26:1704–13.
- [127] Karlsson A, Yi T, Bengtsson P-E. Absorption and scattering of light from ensembles of randomly oriented aggregates. *J Opt Soc Am A* 2013;30:316–24.
- [128] Okada Y, Mukai T, Mann I, Nomura H, Takeuchi T, Sano I, et al. Grouping and adding method for calculating light scattering by large fluffy aggregates. *J Quant Spectrosc Radiat Transfer* 2007;108:65–80.
- [129] Mackowski DW. A simplified model to predict the effects of aggregation on the absorption properties of soot aggregates. *J Quant Spectrosc Radiat Transfer* 2006;100:237–49.
- [130] Liou KN, Takano Y, Yang P. Light absorption and scattering by aggregates: Application to black carbon and snow grains. *J Quant Spectrosc Radiat Transfer* 2011;112:1581–94.
- [131] Mackowski DW. Calculation of total cross sections of multiple-sphere clusters. *J Opt Soc Am A* 1994;11:2851–61.
- [132] Brunning JH, Lo YT. Multiple scattering of em waves by spheres. part I. multiple expansion and ray-optical solutions. *IEEE Trans Antennas Propag* 1971;AP-19:378–90.
- [133] Borghese F, Denti P, Saija R, Toscano G, Sindoni OI. Multiple electromagnetic scattering from a cluster of spheres. I. theory. *Aerosol Sci Technol* 1984;3:227–35.

- [134] Mackowski DW, Mishchenko MI. Calculation of the T matrix and the scattering matrix for ensembles of spheres. *J Opt Soc Am A* 1996;13:2266–78.
- [135] Mishchenko MI. Light scattering by randomly oriented axially symmetric particles. *J Opt Soc Am A* 1991;8:871–82.
- [136] Khlebtsov NG. Orientational averaging of light-scattering observables in the T-matrix approach. *Appl Opt* 1992;31:5359–65.
- [137] Mackowski DW, Mishchenko MI. A multiple sphere T-matrix Fortran code for use on parallel computer clusters. *J Quant Spectrosc Radiat Transfer* 2011;112:2182–92.
- [138] Liu L, Mishchenko MI. Effects of aggregation on scattering and radiative properties of soot aerosols. *J Geophys Res* 2005;110:D11211.
- [139] Liu L, Mishchenko MI, Arnott WP. A study of radiative properties of fractal soot aggregates using the superposition T-matrix method. *J Quant Spectrosc Radiat Transfer* 2008;109:2656–63.
- [140] Kahnert M. On the discrepancy between modelled and measured mass absorption cross sections of light absorbing carbon aerosols. *Aerosol Sci Technol* 2010;44:453–60.
- [141] Yin JY, Liu LH. Influence of complex component and particle polydispersity on radiative properties of soot aggregate in atmosphere. *J Quant Spectrosc Radiat Transfer* 2010;111:2115–26.
- [142] Wu Y, Gu X, Cheng T, Xie D, Yu T, Chen H, et al. The single scattering properties of the aerosol particles as aggregated spheres. *J Quant Spectrosc Radiat Transfer* 2012;113:1454–66.
- [143] Wu Y, Cheng T, Zheng L, Chen H. A study of optical properties of soot aggregates composed of poly-disperse monomers using the superposition T-matrix method. *Aerosol Sci Technol* 2015;49:941–9.
- [144] Wu Y, Cheng T, Zheng L, Chen H, Xu H. Single scattering properties of semi-embedded soot morphologies with intersecting and non-intersecting surfaces of absorbing spheres and non-absorbing host. *J Quant Spectrosc Radiat Transfer* 2015;157:1–13.
- [145] Zhang X, Mao M, Yin Y, Wang B. Absorption enhancement of aged black carbon aerosols affected by their microphysics: a numerical investigation. *J Quant Spectrosc Radiat Transfer* 2017;202:90–7. doi:10.1016/j.jqsrt.2017.07.025.
- [146] Luo J, Zhang Y, Wang F, Wang J, Zhang Q. Applying machine learning to estimate the optical properties of black carbon fractal aggregates. *J Quant Spectrosc Radiat Transfer* 2018;215:1–8.
- [147] Wu Y, Cheng T, Liu D, Allan JD, Zheng L, Chen H. Light absorption enhancement of black carbon aerosol constrained by particle morphology. *Environ Sci Technol* 2018;52(12):6912–19. doi:10.1021/acs.est.8b00636. PMID: 29783837.
- [148] Liu C, Xu X, Yin Y, Schnaiter M, Yung YL. Black carbon aggregates: A database for optical properties. *J Quant Spectrosc Radiat Transfer* 2019;222–223:170–9.
- [149] Purcell EM, Pennypacker CR. Scattering and absorption of light by nonspherical dielectric grains. *Astrophys J* 1973;186:705–14.
- [150] Yurkin MA, Hoekstra AG. The discrete dipole approximation: an overview and recent developments. *J Quant Spectrosc Radiat Transfer* 2007;106:558–89.
- [151] Draine BT, Flatau PJ. Discrete-dipole approximation for scattering calculations. *J Opt Soc Am A* 1994;11:1491–9.
- [152] Yurkin MA, Maltsev VP, Hoekstra AG. The discrete dipole approximation for simulation of light scattering by particles much larger than the wavelength. *J Quant Spectrosc Radiat Transfer* 2007;106:546–57.
- [153] Worringer A, Ebert M, Trautmann T, Weinbruch S, Helas G. Optical properties of internally mixed ammonium sulfate and soot particles—a study of individual aerosol particles and ambient aerosol populations. *Appl Opt* 2008;47:3835–45.
- [154] Kocifaj M, Videen G. Optical behavior of composite carbonaceous aerosols: DDA and EMT approaches. *J Quant Spectrosc Radiat Transfer* 2008;109:1404–16.
- [155] Kahnert M, Nousiainen T, Lindqvist H, Ebert M. Optical properties of light absorbing carbon aggregates mixed with sulfate: assessment of different model geometries for climate forcing calculations. *Opt Express* 2012;20:10042–58.
- [156] Kahnert M, Nousiainen T, Lindqvist H. Models for integrated and differential scattering optical properties of encapsulated light absorbing carbon aggregates. *Opt Express* 2013;21:7974–92.
- [157] Scarnato B, Vahidinia S, Richard DT, Kirchstetter TW. Effects of internal mixing and aggregate morphology on optical properties of black carbon using a discrete dipole approximation model. *Atmos Chem Phys* 2013;13:5089–101.
- [158] Wu Y, Cheng T, Zheng L, Chen H. Effect of morphology on the optical properties of soot aggregated with spheroidal monomers. *J Quant Spectrosc Radiat Transfer* 2016;168:158–69.
- [159] Wu Y, Cheng T, Zheng L, Chen H. Models for the optical simulations of fractal aggregated soot particles thinly coated with non-absorbing aerosols. *J Quant Spectrosc Radiat Transfer* 2016;182:21–11.
- [160] Wu Y, Cheng T, Zheng L, Chen H. Sensitivity of mixing states on optical properties of fresh secondary organic carbon aerosols. *J Quant Spectrosc Radiat Transfer* 2017;195:147–55.
- [161] Ishimoto H, Kudo R, Adachi K. A shape model of internally mixed soot particles derived from artificial surface tension. *Atmos Meas Tech* 2019;12:107–18.
- [162] Yurkin MA, Kahnert M. Light scattering by a cube: accuracy limits of the discrete dipole approximation and the T-matrix method. *J Quant Spectrosc Radiat Transfer* 2013;123:176–83.
- [163] Liu C, Teng S, Zhu Y, Yurkin MA, Yung YL. Performance of the discrete dipole approximation for optical properties of black carbon aggregates. *J Quant Spectrosc Radiat Transfer* 2018;221:98–109.
- [164] Yurkin MA, Maltsev VP, Hoekstra AG. Convergence of the discrete dipole approximation. I. theoretical analysis. *J Opt Soc Am A* 2006;23:2578–91.
- [165] Yurkin MA, Maltsev VP, Hoekstra AG. Convergence of the discrete dipole approximation. II. an extrapolation technique to increase the accuracy. *J Opt Soc Am A* 2006;23:2592–601.
- [166] Schmidt K, Yurkin M, Kahnert M. A case study on the reciprocity in light scattering computations. *Opt Express* 2012;20:23253–74.
- [167] Xu Y. Electromagnetic scattering by an aggregate of spheres. *Appl Opt* 1995;34:4573–88.
- [168] Xu Y, Gustafson B. Experimental and theoretical results of light scattering by aggregates of spheres. *Appl Opt* 1997;36:8026–30.
- [169] Xu Y, Gustafson B. A generalized multiparticle Mie solution: further experimental verification. *J Quant Spectrosc Radiat Transfer* 2001;70:395–419.
- [170] Xu Y, Khlebtsov NG. Orientation-averaged radiative properties of an arbitrary configuration of scatterers. *J Quant Spectrosc Radiat Transfer* 2003;79:1121–37.
- [171] Taflov A. Computational electrodynamics - the finite-difference time-domain method. Boston: Artech House; 1995.
- [172] Cui ZW, Han YP, Li CY. Characterization of the light scattering by ensembles of randomly distributed soot aggregates. *J Quant Spectrosc Radiat Transfer* 2011;112:2722–32.
- [173] Zhao Y, Ma L. Applicable range of the rayleigh-debye-gans theory for calculating the scattering matrix of soot aggregates. *Appl Opt* 2009;48:591–7.
- [174] Mackowski DW. Electrostatics analysis of radiative absorption by sphere clusters in the Rayleigh limit: application to soot particles. *Appl Opt* 1995;34:3535–45.
- [175] Lu N, Sorensen CM. Depolarized light scattering from fractal soot aggregates. *Phys Rev E* 1994;50:3109–15.
- [176] Paulien L, Ceolato R, Soucasse L, Enguehard F, Soufiani A. Lidar-relevant radiative properties of soot fractal aggregate ensembles. *J Quant Spectrosc Radiat Transfer* 2019;106706. doi:10.1016/j.jqsrt.2019.106706.
- [177] Sihvola A. Electromagnetic mixing formulas and applications. London: Institution of Electrical Engineers; 1999.
- [178] Chýlek P, Videen G, Geldart DJW, Dobbie JS, Tso HCW. Effective medium approximations for heterogeneous particles. In: Mishchenko MI, Hovenier JW, Travis LD, editors. Light scattering by nonspherical particles. San Diego: Academic Press; 2000. p. 274–308.
- [179] Maxwell Garnett JC. Colours in metal glasses and in metallic films. *Philos Trans R Soc A* 1904;203:385–420.
- [180] Bruggemann DAG. Berechnung verschiedener physikalischer Konstanten von heterogenen Substanzen. 1. Dielektrizitätskonstanten und Leitfähigkeiten der Mischkörper aus isotropen Substanzen. *Ann Phys* 1935;24:636–664.
- [181] Videen G, Chýlek P. Scattering by a composite sphere with an absorbing inclusion and effective medium approximations. *Opt Commun* 1998;158:1–6.
- [182] Kocifaj M, Kundracik F, Videen G. Optical properties of single mixed-phase aerosol particles. *J Quant Spectrosc Radiat Transfer* 2008;109:2108–23.
- [183] Ackerman TP, Toon OB. Absorption of visible radiation in atmospheres containing mixtures of absorbing and nonabsorbing particles. *Appl Opt* 1981;20:3661–8.
- [184] Fuller KA. Scattering and absorption cross sections of compounded spheres III. spheres containing arbitrarily located spherical inhomogeneities. *J Opt Soc Am A* 1995;12:893–904.
- [185] Mishchenko MI, Liu L, Travis LD, Lacis AA. Scattering and radiative properties of semi-external versus external mixtures of different aerosol types. *J Quant Spectrosc Radiat Transfer* 2004;88:139–47.
- [186] Kandilian R, Heng R-L, Pilon L. Absorption and scattering by fractal aggregates and by their equivalent coated spheres. *J Quant Spectrosc Radiat Transfer* 2015;151:310–26.
- [187] Latimer P. Experimental tests of a theoretical method for predicting light scattering by aggregates. *Appl Opt* 1985;24:3231–9.
- [188] Fuller KA, Malm WC, Kreidenweis SM. Effects of mixing on extinction by carbonaceous particles. *J Geophys Res* 1999;104:15941–54.
- [189] Wu Y, Cheng T, Gu X, Zheng L, Chen H, Xu H. The single scattering properties of soot aggregates with concentric core-shell spherical monomers. *J Quant Spectrosc Radiat Transfer* 2014;135:9–19.
- [190] Kahnert M. Optical properties of black carbon aerosols encapsulated in a shell of sulphate: comparison of the closed cell model with a coated aggregate model. *Opt Express* 2017;25:2479–93.
- [191] Liu L, Mishchenko MI. Scattering and radiative properties of morphologically complex carbonaceous aerosols: A systematic modeling study. *Remote Sensing* 2018;10.
- [192] Luo J, Zhang Y, Wang F, Zhang Q. Effects of brown coatings on the absorption enhancement of black carbon: a numerical investigation. *Atmos Chem Phys* 2018;18(23):16897–914. doi:10.5194/acp-18-16897-2018.
- [193] Luo J, Zhang Y, Zhang Q, Wang F, Liu J, Wang J. Sensitivity analysis of morphology on radiative properties of soot aerosols. *Opt Express* 2018;26(10):A420–32. doi:10.1364/OE.26.00A420.
- [194] Luo J, Zhang Y, Zhang Q. A model study of aggregates composed of spherical soot monomers with an acentric carbon shell. *J Quant Spectrosc Radiat Transfer* 2018;205:184–95. doi:10.1016/j.jqsrt.2017.10.024.
- [195] Bond TC, Habib G, Bergstrom RW. Limitations in the enhancement of visible light absorption due to mixing state. *J Geophys Res* 2006;111. doi:10.1029/2006JD007315. D20211.
- [196] Cappa CD, Zhang X, Russell LM, Collier S, Lee AKY, Chen C-L, et al. Light absorption by ambient black and brown carbon and its dependence on black carbon coating state for two california, usa, cities in winter and summer. *J Geophys Res* 2019;124(3):1550–77. doi:10.1029/2018JD029501.

- [197] Chakrabarty RK, Heinson WR. Scaling laws for light absorption enhancement due to nonrefractory coating of atmospheric black carbon aerosol. *Phys Rev Lett* 2018;121:218701. doi:10.1103/PhysRevLett.121.218701.
- [198] Li J, Liu C, Kumar YYNKR. Numerical investigation of the ångström exponent of black carbon aerosol. *J Geophys Res Atmos* 2016;121:3507–18.
- [199] Liu C, Li J, Yin Y, Zhu B, Feng Q. Optical properties of black carbon aggregates with non-absorptive coating. *J Quant Spectrosc Radiat Transfer* 2017;187:443–52. doi:10.1016/j.jqsrt.2016.10.023.
- [200] Kanngießer F, Kahnert M. Coating material-dependent differences in modelled lidar-measurable quantities for heavily coated soot particles. *Opt Express* 2019;27:36368–87.
- [201] Burton SP, Hair JW, Kahnert M, Ferrare RA, Hostetler CA, Cook AL, et al. Observations of the spectral dependence of particle depolarization ratio of aerosols using NASA Langley airborne High Spectral Resolution Lidar.. *Atmos Chem Phys* 2015;15:13453–73.
- [202] Mishchenko MI, Dlugach JM, Liu L. Linear depolarization of lidar returns by aged smoke particles. *Appl Opt* 2016;55(35). doi:10.1364/AO.55.009968.
- [203] Mishchenko MI, Sassen K. Depolarization of lidar returns by small ice crystals: An application to contrails. *Geophys Res Lett* 1998;25:309–12.
- [204] Bi L, Lin W, Liu D, Zhang K. Assessing the depolarization capabilities of nonspherical particles in super-ellipsoidal shape space. *Opt Express* 2018;26:1726–42.
- [205] Kahnert M, Andersson E. How much information do extinction and backscattering measurements contain about the chemical composition of atmospheric aerosol. *Atmos Chem Phys* 2017;17:3423–44.
- [206] Kahnert M. Information constraints in variational data assimilation. *Q J R Meteorol Soc* 2018;144:2230–44.
- [207] Ward E. Use of remote sensing and in situ observations of the atmosphere in chemical transport models. Chalmers University of Technology; 2019.
- [208] Mishchenko MI, Travis LD, Kahn RA, West RA. Modeling phase functions for dustlike tropospheric aerosols using a shape mixture of randomly oriented polydisperse spheroids. *J Geophys Res* 1997;102 16,831–16,847.
- [209] Merikallio S, Lindqvist H, Nousiainen T, Kahnert M. Modelling light scattering by mineral dust using spheroids: assessment of applicability. *Atmos Chem Phys* 2011;11:5347–63.